Hydrogen and oxygen trapping at the H-cluster of [FeFe]-hydrogenase revealed by site-selective spectroscopy and QM/MM calculations

Stefan Mebs[1], Ramona Kositzki[1], Jifu Duan[2], Moritz Senger[3], Florian Wittkamp[4], Ulf-Peter Apfel[4], Thomas Happe[2], Sven T. Stripp[3], Martin Winkler[2*], and Michael Haumann[1*]

[1]Department of Physics, Biophysics of Metalloenzymes, Freie Universität Berlin, 14195 Berlin, Germany

[2]Department of Biochemistry of Plants, Photobiotechnology, Ruhr-Universität Bochum, 44801 Bochum, Germany

[3]Department of Physics, Experimental Molecular Biophysics, Freie Universität Berlin, 14195 Berlin, Germany

[4]Department of Chemistry and Biochemistry, Inorganic Chemistry I, Ruhr-Universität Bochum, 44801 Bochum, Germany

Correspondence to:

Dr. Michael Haumann, Freie Universität Berlin, Fachbereich Physik, Arnimallee 14, 14195 Berlin, Germany, Phone: +49 30 838 56101, Email: michael.haumann@fu-berlin.de

Dr. Martin Winkler, Ruhr-Universität Bochum, Universitätsstrasse 150, 44801 Bochum, Germany, +49 234 3227 049, Email: martin.winkler-2@rub.de

Running Title: Hydrogen and oxygen trapping in [FeFe]-hydrogenase

Keywords: [FeFe]-hydrogenase, H-cluster, ligand binding, site-selective spectroscopy, QM/MM

Abbreviations: [2Fe] and [4Fe4S], diiron and four-iron sub-complexes of the H-cluster; adt, azadimethyldithiolate; CPI, [FeFe]-hydrogenase from *Clostridium pasterianum*; ctv, core-to-valence transition; HYDA1, [FeFe]-hydrogenase protein from *C. reinhardtii*; DFT, density functional theory; Fe_p and Fe_d, proximal and distal iron ions in [2Fe]; FTIR, Fourier-transform infrared spectroscopy; NFS, nuclear forward scattering; NIS; nuclear inelastic scattering; NRVS, nuclear resonance vibrational spectroscopy; PDOS, partial density of states; QM/MM, quantum mechanics/molecular mechanics; vtc, valence-to-core transition; XAS/XES, X-ray absorption/emission spectroscopy; XANES, X-ray absorption near edge structure

Abstract

[FeFe]-hydrogenases are superior hydrogen conversion catalysts. They bind an active-site cofactor (H-cluster) comprising a four-iron and a diiron unit with three carbon monoxide (CO) and two cyanide (CN^-) ligands. Hydrogen (H_2) and oxygen (O_2) binding at the H-cluster was studied in the C169A variant of [FeFe]-hydrogenase HYDA1, in comparison to the active oxidized (**Hox**) and CO-inhibited (**Hox-CO**) species in wildtype enzyme. ^{57}Fe labeling of the diiron site was achieved by in vitro maturation with a synthetic analogue ($^{57}Fe_2$(μ-adt)$(CO)_4(CN^-)_2$, adt = $(SCH_2)_2NH$). Site-selective X-ray absorption, emission, and nuclear inelastic/forward scattering methods and infrared spectroscopy were combined with quantum chemical calculations to determine the molecular and electronic structure and vibrational dynamics of detected cofactor species. **Hox** reveals an apical vacancy at Fe_d in a $[4Fe4S\text{-}2Fe]^{3-}$ complex with the net spin on Fe_d whereas **Hox-CO** shows an apical CN^- at Fe_d in a $[4Fe4S\text{-}2Fe(CO)]^{3-}$ complex with net spin sharing among Fe_p and Fe_d (proximal or distal iron ions in [2Fe]). At ambient O_2 pressure, a novel H-cluster species (**Hox-O_2**) accumulated in C169A, assigned to a $[4Fe4S\text{-}2Fe(O_2)]^{3-}$ complex with an apical superoxide (O_2^-) ligand carrying the net spin bound at Fe_d. H_2 exposure populated a two-electron reduced species (**HhydH**) in C169A, assigned as a $[(H)4Fe4S\text{-}2Fe(H)]^{3-}$ complex with the net spin on the reduced cubane, an apical hydride at Fe_d, and a proton at a sulfur atom of a cysteine ligand. **Hox-O_2** and **HhydH** are stabilized by impaired O_2^- protonation or proton release after H_2 cleavage due to interruption of the proton path towards and out of the active site. Protonation at the H-cluster is essential in O_2-induced cofactor degradation and H_2 conversion in [FeFe]-hydrogenases.

Introduction

Hydrogen (H_2) is an attractive fuel for a sustainable and carbon-free future energy economy [1, 2]. However, efficient synthetic H_2 conversion catalysts based on abundant transition metals are relatively rare [3, 4]. [FeFe]-hydrogenases are nature´s most effective H_2 conversion catalysts [5-7]. Their active site consists of a six-iron cofactor (H-cluster), which represents a potential blueprint for chemical systems [8-12]. The interrelations between redox chemistry and protolytic events during H_2 conversion and oxygen (O_2) induced inactivation at the cofactor thus need to be understood. The smallest [FeFe]-hydrogenase, HYDA1 from *Chlamydomonas reinhardtii*, carries only the H-cluster [7, 13], but no further relay iron-sulfur clusters as bacterial enzymes. It therefore is superior for spectroscopic studies on the mechanism. Crystallography has indicated that the H-cluster structure is alike in all [FeFe]-hydrogenase types [14-16].

The H-cluster comprises a canonical cubane-type iron-sulfur cluster, [4Fe4S], which is covalently linked to a unique diiron complex, [2Fe] (Fig. 1). The two iron ions of [2Fe] (in distal, d, or proximal, p, positions relative to [4Fe4S]) are connected by an aza-dimethyl-dithiolate molecule (adt = $(SCH_2)_2NH$) and bind two terminal carbon monoxide (CO) and cyanide (CN^-) ligands, as well as a metal-bridging CO (μCO) in the oxidized state (**Hox**) of the cofactor [16-18]. Binding of an exogenous CO ligand at Fe_d to form **Hox-CO** reversibly inhibits H_2 turnover activity [19, 20]. Exposure of [FeFe]-hydrogenases in solution to O_2 causes rapid cofactor degradation [21-23]. Based on the O_2 resistance of freeze-dried enzymes and kinetic studies, the deleterious O_2 effects may be coupled to proton transfer [24-28].

The cofactor is embedded in a hydrogen-bonded network of amino acids and water molecules (Fig. 1) [7, 16, 29], which provides conserved proton pathways to the cofactor [7, 29-32]. In particular, the amino acid Cys169 is crucial for proton transfer, because exchange of Cys169 against alanine (C169A) results in an inactive enzyme [32]. H-bonding and protein vibrational dynamics may also be involved in determining the orientation in the binding

pocket and coordination geometry of the cofactor during substrate and inhibitor binding [7, 20, 33]. Spectroscopic studies have revealed a variety of H-cluster species that emerge upon reduction of **Hox**. One-electron reduced (**Hred**, **Hred´**) and two-electron reduced species (**Hsred**, "**Hhyd**") were discriminated [29, 30, 34-43]. How these species are involved in the catalytic cycle, however, is still under debate. The two-electron reduced species have been proposed to bind hydride at [2Fe], either in the metal-bridging (**Hsred**) or in apical position at Fe_d ("**Hhyd**") [30, 35, 37, 38, 40, 42]. Further protonation events at the H-cluster as in [NiFe]-hydrogenases are conceivable [44-48]. We have previously assigned protonation at [4Fe4S] in **Hred´**, as well as in equivalents of the oxidized and CO-inhibited H-cluster species, which are formed at acidic pH [29].

Reduction and protonation in the catalytic cycle at either [4Fe4S] or [2Fe] implies that site-selective molecular biology and spectroscopic techniques are valuable for reaction site discrimination. Mutagenesis of Cys169 results in protein variants with a defective proton path [7, 30, 32]. For C169A and other variants of HYDA1, enrichment of "**Hhyd**" has been observed under certain conditions [30, 35, 40, 42]. In HYDA1 and bacterial enzymes, both sub-complexes can be functionally reconstituted in vitro with inorganic [4Fe4S] precursors and synthetic [2Fe] analogues, which facilitates selective isotope labeling, e.g., with ^{57}Fe [40, 49-54]. Thereby, site-selective studies become feasible, using methods, which monitor only ^{57}Fe nuclei, such as Mössbauer spectroscopy and nuclear inelastic scattering (NIS) techniques at synchrotron radiation sources [40, 55, 56]. NIS provides quadrupole splitting energies (ΔE_Q) from nuclear forward scattering (NFS) and vibrational cofactor and protein modes from nuclear resonance vibrational spectroscopy (NRVS) [40, 57-59]. Investigation of vibrations of the diatomic [2Fe] ligands is facilitated by Fourier-transform infrared (FTIR) and Raman spectroscopy [20, 34, 43, 60, 61]. Utilizing the different spin states of iron species in the H-cluster, i.e. high-spin Fe(II)/Fe(III) in [4Fe4S] or low-spin Fe(I)/Fe(II) in [2Fe], high-resolution X-ray absorption and emission spectroscopy (XAS/XES) facilitates site-selective

investigation of molecular and electronic structures of the sub-complexes [36, 37, 62, 63]. FTIR, NFS/NRVS, and XAS/XES methods are sensitive to all possible spin and redox states of the cofactor.

Here, in-vitro reconstitution of HYDA1 with a ^{57}Fe-labeled [2Fe] precursor was combined with site-selective X-ray and IR spectroscopy. Quantum chemical calculations were employed for spectral simulation. Hydrogen and oxygen binding, as well as redox, protonation, and vibrational dynamics changes at the H-cluster were investigated in C169A in comparison to **Hox** and **Hox-CO** in WT. Trapping of a superoxide molecule (O_2^-) at the diiron site occurs in C169A (**Hox-O_2**). A terminal hydride in [2Fe] and an additional protonation at [4Fe4S] were assigned to a double-reduced species (**HhydH**). Four-iron and/or diiron site protonation is essential for O_2-induced cofactor degradation and H_2 turnover.

Materials and Methods

Protein sample preparation. [FeFe]-hydrogenase HYDA1 apo-protein containing only the cubane cluster was over-expressed in *Escherichia coli* BL21 Δ-IscR [64], purified, and quantitatively reconstituted in vitro with a synthetic diiron complex ($2Fe_{adt}$ = Fe_2(μ-adt)$(CO)_4(CN)_2$) to form the fully active [2Fe] sub-complex, as previously described [52, 54]. $2Fe_{adt}$ was synthesized with ^{56}Fe or ^{57}Fe following established routes [52-54]. Selective ^{57}Fe labeling of the H-cluster was achieved (i) by removal of the iron and sulfur ions of the native cluster in apo-HYDA1 and subsequent reconstitution of [4Fe4S] with sulfide and ^{57}Fe (using a $^{57}Fe^{II}Cl_2$ solution). Maturation with $2^{56}Fe_{adt}$ yielded [4^{57}Fe4S-2^{56}Fe] while addition of $2^{57}Fe_{adt}$ resulted in [4^{57}Fe4S-2^{57}Fe]. (ii) Alternatively, apo-HYDA1 containing [4^{56}Fe4S] was maturated with $2^{56}Fe_{adt}$ to yield [4^{56}Fe4S-2^{56}Fe] or with $2^{57}Fe_{adt}$ to yield [4^{56}Fe4S-2^{57}Fe], as described earlier [35, 52-54]. Protein samples of HYDA1 WT and variant C169A were prepared as previously described [7]. All protein preparation and handling procedures were carried out under strictly anoxic conditions and dim light if not stated otherwise. **Hox** was

near-quantitatively populated in as-isolated WT protein (~2mM, 50 µL) by flushing for ~30 min with N_2 gas humidified with buffer solution (pH 8.0). **Hox-CO** was accumulated by flushing HYDA1 in **Hox** with CO gas for ~30 min. C169A as prepared under reducing conditions (1 % H_2) contained mainly **HhydH** (previously denoted "**Hhyd**") [35, 40, 42]. This intermediate was further enriched by exposure of samples (~2 mM, ~50 µl, pH 8) to H_2 gas for 15 min. **Hox-O_2** was populated in C169A by exposure of as-isolated protein in buffer solution (~2 mM, ~50 µL, pH 8.0) to air (~21 % O_2) for ~5 min under gentle stirring.

FTIR spectroscopy. Fourier-transform infrared spectroscopy was performed on hydrogenase protein films (1 µl) in attenuated total reflection (ATR) geometry on a Tensor27 spectrometer (Bruker) in an anaerobic glove box as previously described [20, 29]. FTIR spectra were evaluated using in-house software and least-squares fit algorithms [20, 29].

X-ray absorption and emission spectroscopy. X-ray absorption (XAS) and emission (XES) spectra at the Fe K-edge were collected at undulator beamline ID26 at the European Synchrotron Radiation Facility (ESRF, Grenoble, France) [36, 37]. Samples were held in a liquid-He cryostat (Cryovac) at 20 K. The excitation energy was set by a Si[311] double-crystal monochromator (energy bandwidth ~0.2 eV). The spot size on the samples was set by slits to ~0.2 mm vertical and 0.3-0.5 mm horizontal. Conventional Fe K-edge absorption spectra were collected within ~5 s scans (rapid scan mode of ID26) using broad-band monitoring of the total (Kα) X-ray fluorescence with a scintillation detector shielded by 10 µm Mn foil against scattered X-rays. A vertical-plane Rowland-circle spectrometer and an avalanche photodiode (APD) detector were used for monitoring of the non-resonantly excited (7800 eV) Kβ X-ray fluorescence. An energy bandwidth of ~1.0 eV at the Fe Kβ fluorescence lines was achieved using the Ge[620] Bragg reflections of 5 spherically-bent Ge wafers (R = 1000 mm). The energy axis of the monochromator was calibrated (accuracy ±0.1 eV) using the K-edge spectrum of an iron metal foil (reference energy 7112 eV in the first derivative spectrum). The energy axis of the emission spectrometer was calibrated (accuracy ±0.1 eV)

using a Gaussian fit to the elastic scattering peak of the energy-calibrated excitation beam. Kβ main line (Kβ′ and $K\beta_{1,3}$) spectra were collected using spectrometer step-scanning (~5 s X-ray exposure, 0.3 eV steps, ~10 spectra from separate sample spots averaged for signal-to-noise ratio improvement). Kβ satellite line ($K\beta_{2,5}$) emission spectra were collected using the previously described energy-sampling approach (energy step size of 0.3 eV, ~5 s data acquisition per sample spot, 5-7 data sets averaged) [57, 65]. A rapid shutter blocked the incident X-rays during emission spectrometer movements. Site-selective Fe K-edge absorption spectra in the XANES or pre-edge regions were measured using $K\beta_{1,3}$ (7060 eV) or Kβ′ (7045 eV) emission detection (averaging of up to ~100 scans, 5 scans of ~2 s duration per sample spot) [63, 66]. Kβ detected pre-edge spectra were normalized by scaling to XANES amplitudes. XAS/XES data were processed and evaluated using established procedures and in-house software [36, 37, 66, 67].

Nuclear resonance spectroscopy. Nuclear resonance vibrational spectroscopy (NRVS) and nuclear forward scattering (NFS) data were collected at undulator beamline ID18 at the ESRF using the previously described set-up including a heat-load monochromator, a high-resolution monochromator (FWHM ~0.7 meV), gated APD detectors for delayed inelastic and forward scattering detection with sub-nanosecond time resolution, and a cold-finger liquid-helium cryostat (sample temperature of 50±7 K) [57]. The storage ring was operated in 16-bunch mode (~90 mA). NRVS spectra were collected in a -15 meV to 110 meV energy region around the resonance (0.2 meV steps, 3 s per data point, spot size on sample ~1.5x0.5 mm^2) and up to 40 scans were averaged (5 scans of ~30 min per sample spot). NFS traces were collected in a ~160 ns time window within ~30 min with the APD detectors at ~2 m behind the sample. NRVS data were processed and the partial vibrational density of states (PDOS) was calculated with the software package available at ID18. NFS traces showed rapid intensity (I) decrease related to the ^{57}Fe excited state lifetime (τ_0 = 141 ns) and superimposed

oscillations due to interference of forward scattering from the I = 3/2 and I = 1/2 nuclear excitation levels, separated by the quadrupole splitting energy (ΔE_Q), which was calculated by Eq. 1 (A = amplitude scaling factor, τ = effective decay lifetime, υ = modulation frequency, φ = phase shift, B = detector count offset) and using $\Delta E_Q = h\upsilon$ ($h = 4.135 \times 10^{-6}$ neVs) [68, 69].

(1) $I_{NFS}(t) = A\exp(-t/\tau)\cos^2(\pi\upsilon t + \varphi) + B$.

The apparent Mössbauer linewidth (Γ) was calculated from τ using Eq. 2:

(2) $\Gamma = h/2\pi(1/\tau_0 + 1/\tau)$.

In-house software and functionalized EXCEL-sheets were used to evaluate metal/ligand contributions to XAS/XES and NRVS spectra. Molecular orbitals, spin density distributions, and vibrational modes were visualized with ChemCraft.

QM/MM and DFT calculations. Calculations were carried out on the Soroban and Sheldon computer clusters of the Freie Universität Berlin. They involved model structures as constructed using crystal structures of [FeFe]-hydrogenase CPI from *Clostridium pasteurianum* (PDB entry 4XDC, 1.63 Å resolution)[16] and of HYDA1 apo-protein (PDB entry 3LX4, 1.97 Å resolution) [70] as previously described [29] (Fig. S1). For large model structures (truncated CPI structure resembling the structure of apo-HydA1 and lacking accessory FeS clusters), a quantum mechanics/molecular mechanics (QM/MM) approach including ONIOM [71, 72] and the universal force field as implemented in Gaussian09 [73] were used for the MM treatment of the protein environment (low-layer) and the TPSSh or BP86 functional with the TZVP basis-set [74-77] were used for the QM core (high-layer including the H-cluster and adjacent amino acids) for unconstraint geometry-optimization. For small model structures (including the H-cluster and adjacent amino acids in some cases; the cysteine ligands of the H-cluster were represented by SCH_3 groups), DFT (TPSSh or BP86 functional and TZVP basis-set) was applied for geometry-optimization. A broken-symmetry approach and proper assignment of molecular fragments were used for calculation of anti-

ferromagnetic spin couplings. For **Hox**, the total spin multiplicity (M = 2S+1) was 3 and the total charge of the H-cluster was -3. For other species, multiplicities and charges reflected the number of added electrons and protons. Vibrational frequencies were derived from normal mode analysis of relaxed structures using Gaussian09, which yielded IR spectra. NRVS/PDOS spectra were calculated using NISspec [78]. Mulliken spin densities and CM5 charges were calculated with Gaussian09 for the DFT models and the QM/MM high-layer. Pre-edge absorption (ctv) and Kβ satellite emission (vtc) spectra were derived from spin-unrestricted single-point DFT calculations or ctv spectra were calculated by time-dependent DFT (TDDFT) on relaxed structures using ORCA (COSMO solvation model, ε = 4) [79]. To calculated ctv or vtc stick spectra, Gaussian broadening (FWHM 1 eV or 3 eV) was applied and spectra were shifted by ~150 eV for alignment with experimental spectra, calculated IR spectra were broadened with FWHM values derived from fits of experimental spectra using Voigt functions (50 % Gaussian and Lorentzian characters), and calculated vibrational modes in PDOS data were broadened by Lorentzians (FWHM 8 cm^{-1}). Root-mean-square deviations (rmsd) for correlations of calculated and experimental IR frequencies (F) were derived from Eq. 3 (n = number of CO plus CN^- ligands, see legend of Fig. 3 for the definition of F_i^{cor}) [29]:

$$(3)\quad rmsd = \sqrt{\sum_{1-n}^{i}\left(F_i^{\exp} - F_i^{cor}\right)^2 / n} \quad .$$

Results

H-cluster redox state. Wildtype (WT) and C169A variants of [FeFe]-hydrogenase HYDA1 apo-protein were reconstituted in vitro with a ^{57}Fe-labeled synthetic diiron site analogue ($^{57}Fe_2(\mu\text{-adt})(CO)_4(CN)_2$) [35, 40, 52, 54]. In WT, oxidized (**Hox**) or carbon monoxide inhibited (**Hox-CO**) H-cluster species were enriched (see Materials and Methods). Exposure of C169A to O_2 or H_2 gas resulted in preferential population of species further on denoted as **Hox-O_2** or **HhydH**. XANES spectra at the Fe K-edge of WT and C169A (^{56}Fe) are

shown in Fig. 2A. The K-edge energy (~7119.7 eV) of the broad-band Kα-detected XANES of **Hox** (Table 1) was similar to earlier data [37]. **Hox-O_2** showed a ~0.6 eV higher energy vs. **Hox**, suggesting apparent one-electron oxidation of about one of the six iron ions in the H-cluster. **HhydH** showed a ~0.7 eV lower K-edge energy vs. **Hox**, suggesting reduction of at least one iron ion. Non-resonantly excited Kβ main-line emission spectra are shown in Fig. 2B. While their overall shape was similar for WT and C169A, the $K\beta_{1,3}$ line energy vs. **Hox** was ~0.1 eV increased for **Hox-O_2**, but ~0.1 eV decreased for **HhydH** (Table 1), corroborating iron oxidation or reduction. Significant Kβ′ intensity changes were not observed, meaning that the [2Fe] iron ions in **Hox**, **Hox-O_2**, and **HhydH** were in the low-spin state [37, 66, 80]. Narrow-band Kβ-detected XANES spectra provide significant site-selectivity because the $K\beta_{1,3}$- or Kβ′-detected XANES is dominated by the high-spin iron ions in [4Fe4S] or the low-spin iron ions in [2Fe] in the pre-edge absorption and low-energy K-edge regions [36, 37, 63]. For $K\beta_{1,3}$-detection, the K-edge energy of **Hox-O_2** was slightly (~0.2 eV) increased and the edge energy of **HhydH** was significantly (~0.6 eV) decreased whereas for Kβ′-detection, the K-edge energy of **Hox-O_2** was significantly (~0.9 eV) increased and the edge energy of **HhydH** was less pronouncedly (~0.3 eV) increased relative to **Hox** (Fig. 2A, Table 1). These results suggested that in **Hox-O_2** mostly iron in [2Fe] became oxidized while **HhydH** showed less pronounced oxidation of iron in [2Fe] and preferential reduction of iron in [4Fe4S].

Infrared vibrational spectroscopy. FTIR spectra were recorded on aliquots of the HYDA1 samples used for X-ray spectroscopy. H-cluster species populations were quantified by fit analysis (Fig. S2) [20, 29]. This analysis revealed ~92 % **Hox** or ~84 % **Hox-CO** in WT and ~89 % **Hox-O_2** or ~81 % **HhydH** in C169A (estimated error ±5 %). Pure IR spectra of the dominant H-cluster species in WT and C169A are shown in Fig. 3A. Relative intensities

and frequencies of the IR bands due to stretching vibrations of the diatomic ligands in [2Fe] revealed the typical pattern of the CO (α, β, γ) and CN^- (ε, ζ) vibrations of **Hox** (Table 2) [20, 29]. **Hox-CO** showed the well-known band frequencies/intensities and an additional band δ [20]. **Hox-O_2** showed an overall similar IR intensity pattern with broadened bands, but large (mean of ~50 cm^{-1}) frequency up-shifts of all CO bands and significant (mean of ~15 cm^{-1}) up-shifts of both CN^- bands vs. **Hox**. **HhydH** exhibited a similar band pattern as described earlier for, e.g., C169A and WT HYDA1 [29, 35], including broadened bands vs. **Hox** and ~2-fold smaller frequency up-shifts of CO bands β and γ, but similar up-shift of the μCO band α, as well as smaller CN^- band shifts vs. **Hox-O_2**.

Calculation of IR bands. DFT and QM/MM were used for the assignment of IR spectra. We compared different model sizes (Fig. S1), which either comprised only the H-cluster or also neighboring amino acids and the protein environment. A pure (BP86) or a hybrid (TPSSh) DFT functional (TZVP basis set) were used for the H-cluster core and the ONIOM [71, 72] QM/MM approach accounted for the protein. For **Hox**, DFT (TPSSh) on a small H-cluster model provided best agreement of theoretical and experimental IR frequencies. Amino acid or protein inclusion did not improve the result (Fig. S3). IR changes between H-cluster species were generally conservative at all theory levels. Calculated IR spectra for **Hox**, **Hox-CO**, **Hox-O_2**, and **HhydH** are shown in Fig. 3B. Mean IR frequency shifts and root-mean-square deviations (rmsd, Eq. 3) between calculated and experimental CO/CN^- frequencies are given in Tables 2 and 3. **Hox** (rmsd ~8 cm^{-1}) comprises a μCO ligand and an apical vacancy at Fe_d as in crystal structures [16]. **Hox-CO** is best described with an apical CN^- instead of a CO at Fe_d (rmsd ~11 cm^{-1}) (Fig. 3B,C) [20, 29].

The calculated IR spectrum for a **Hox-O_2** structure with the same redox state as **Hox** and an O_2 molecule bound end-on to Fe_d nicely reproduced the experimental spectrum (rmsd

~11 cm^{-1}) (Fig. 3B,C, Tables 2, 3). The band shifts thus reflect decreased electron density at the [2Fe] iron ions due to binding of a formal superoxide (O_2^-) at Fe_d, in agreement with the XANES data. The spectrum for a hydro-peroxo ligand (OOH) was incompatible with the **Hox-O_2** data (Fig. S4). Calculated IR spectra for two-electron reduced structures with a μCO and an apical vacancy at Fe_d or an apical CO at Fe_d and vacant bridging position showed strongly shifted CO bands and altered intensity patterns vs. **Hox**, which disagree with the experimental data of **HhydH** (Fig. S5). The spectrum of a structure with a μH and an apical CO at Fe_d matched the experimental **Hsred** spectrum [38] (Fig. S5), supporting a bridging hydride in **Hsred** [37]. In contrast, a structure with an apical protonation at Fe_d and a μCO produced an IR spectrum closer to **HhydH** (Table 3), supporting a non-bridging hydride at Fe_d, but the CO band shifts still were underestimated (Figs. 3 and S6). The larger experimental band shifts for **HhydH** apparently required a further protonation. We tested conceivable protonation sites at the μS and S(cys) atoms of [4Fe4S] and the μS(adt) and HN(adt) groups of [2Fe] (protonation at the triple-coordinated bridging cysteine was unlikely). Protonation at μS(adt) or HN(adt) resulted in inferior shifts in particular of the μCO band (α) (Fig. S6, Table 3). Protonation at a μS atom of [4Fe4S] yielded reasonable IR patterns, but resulted in distorted cubane structures and therefore was less likely [29]. S(cys) protonation caused further up-shifts of all CO bands (Fig. 3B,C, Tables 2, 3), in good agreement with the **HhydH** spectrum (rmsd ~11 cm^{-1}), and preserved the cubane geometry. Notably, an equatorial hydride and apical CN^- at Fe_d and a proton at μS or S(cys) caused excessively high μCO frequencies. These results assigned **HhydH** to a two-electron reduced H-cluster with a μCO ligand, an apical hydride at Fe_d, and a further proton at a cysteine ligand of [4Fe4S]. Cys417 (S9) in HYDA1 was the favoured protonation site in **HhydH**, as previously found for, e.g., **Hred´** [29].

Normal mode analysis correlated experimental IR bands to individual diatomic ligand vibrations (p, d, μ denotes CO/CN^- at Fe_p, Fe_d, or in the metal-bridging position) (Fig. 3D).

For **Hox**, the largely uncoupled modes belong to μCO (α), dCO (β), pCO (γ), dCN^- (ε), and pCN^- (ζ). **Hox-CO** with an apical CN^- at Fe_d showed an uncoupled μCO (α), coupled modes of the two dCO ligands (β and δ), a more isolated pCO mode (γ), and uncoupled pCN^- (ε) and dCN^- (ζ) vibrations. For **Hox-O_2**, uncoupled μCO (α) and dCO (β) vibrations and a more coupled mode with pCO and dCO contributions (γ), an inverted frequency pattern of pCN^- (ε) and dCN^- (ζ), and an uncoupled O_2^- ligand were observed. **HhydH** revealed vibrational coupling of the hydride with μCO (α) and dCO (β), a coupled mode with hydride/dCO/pCO contributions (γ), and a similar CN^- frequency inversion as **Hox-O_2**, but with hydride coupling to dCN^- (Fig. 3D). Notably, the calculations on **HhydH** structures yielded a further hydride mode with very weak intensity at ≥50 cm^{-1} lower frequency than the μCO band. The experimental **HhydH** spectrum did not show significant narrow bands in this frequency range.

Nuclear resonance vibrational spectroscopy. Vibrational modes with contributions from ^{57}Fe nuclei were probed by NRVS on labeled HYDA1 variants. The (normalized) partial vibrational density of states (PDOS) spectra derived from NRVS spectra of **Hox-CO** for ^{57}Fe labeling at [4Fe4S], [2Fe], or both sub-complexes showed that vibrational modes of [4Fe4S] were prominent at <400 cm^{-1} and absent at higher frequencies whereas modes of [2Fe] dominated at >400 cm^{-1}. The stoichiometric sum of the spectra of the [4^{57}Fe4S] or [2^{57}Fe] constructs matched the spectrum of the completely ^{57}Fe labeled H-cluster (Fig. S7), showing that both sub-complexes were quantitatively incorporated. NRVS spectra of **Hox**, **Hox-CO**, **Hox-O_2**, and **HhydH** and difference spectra for HYDA1 labeled with ^{57}Fe only at [2Fe] are shown in Fig. 4. Particularly prominent and globally similar spectral differences were observed in the 150-300 cm^{-1} and 400-650 cm^{-1} regions due to transition from a (distorted) square-pyramidal Fe_d site in **Hox** to a near-octahedral Fe_d site in **Hox-CO**, **Hox-O_2**, and **HhydH**. QM/MM or DFT were used for calculation of NRVS spectra. QM/MM revealed a

continuum of weak vibrational modes with H-cluster and protein contributions and decreasing intensities at increasing frequencies, accounting for the spectral background of experimental NRVS data (Fig. 4). The spectra from DFT lacked such a background, but otherwise yielded similar specific band features of the H-cluster species as QM/MM (Fig. S8).

The calculated NRVS of **Hox** reasonably reproduced three prominent groups of bands around 250 cm^{-1}, 450 cm^{-1}, and 550-650 cm^{-1} in the experimental spectrum, facilitating the assignment of vibrational modes (Fig. 4). Bands around ~250 cm^{-1} are dominated by adt and cysteine bridge contributions, bands around ~450 cm^{-1} reflect modes with prominent CN^- contributions, and 550-650 cm^{-1} bands are due to coupled CO vibrations (Fig. 4D). The **Hox-CO** spectrum for an apical CN^- vs. an apical CO at Fe_d differed mainly by more even intensities around ~200 cm^{-1} and higher intensities around ~400 cm^{-1} and ~650 cm^{-1}. The experimental **Hox-CO** spectrum and the **Hox-CO** – **Hox** difference for an apical CN^- thus were in better agreement with the experiment. Spectral differences of **Hox-CO** vs. **Hox** are mainly due to ~50 cm^{-1} down-shifts of adt/bridging-cysteine modes, enhanced adt contributions to down-shifted CN^- modes, shifts of more extensively coupled CO modes, and enhanced intensities of adt/CO coupled modes. The NRVS of **Hox-O_2** differed from **Hox** in showing broadened bands around 150-350 cm^{-1} and ~450 cm^{-1} and increased intensity around 600 cm^{-1}, which was nicely reproduced by the calculations (Fig. 4B). Increased intensities of coupled adt/bridging-cysteine/CO/CN^- vibrations account for the spectral broadening at ~200-350 cm^{-1}, down-shifted CN^-/O_2^- modes cause spectral changes at ~400-500 cm^{-1}, and more extensive adt/CO coupling explain the band-shifts at higher frequencies (Fig. 4D).

The NRVS of **HhydH** vs. **Hox** showed significant band shifts around 250 cm^{-1} and 550 cm^{-1}, decreased intensities at ~450 cm^{-1}, and increased intensities at ~650 cm^{-1} (Fig. 4C). The NRVS for only an apical hydride at Fe_d reproduced the main spectral differences already reasonably well. Adding a further proton at S9 of [4Fe4S] caused increased intensity at ~250 cm^{-1} and decreased intensity at ~550 cm^{-1} and provided even better agreement of the **HhydH**

– **Hox** difference with the experimental data (Fig. S8). **HhydH** spectra from all theoretical approaches and irrespective of a second-site protonation revealed small bands around 750 cm^{-1}, due to vibrational modes of the hydride (Fig. S9) [40]. The experimental **HhydH** spectrum showed weak intensities close to the noise level in this region. The **HhydH** vs. **Hox** NRVS difference can be explained by small shifts of modes with adt/bridging-cysteine contributions (~250 cm^{-1}), minor shifts of CN^- modes (~450 cm^{-1}), hydride contributions to CO vibrations (~500-600 cm^{-1}), and significant intensities of hydride/adt/CO modes at ~620 cm^{-1} (Fig. 4D).

Nuclear forward scattering. From NFS time-traces of HYDA1 variants with ^{57}Fe labeled [2Fe], nuclear quadrupole splitting energies (ΔE_Q) and apparent Mössbauer linewidths (Γ, here representing the approximate mean value over the Fe_p and Fe_d ions) were derived from fit analysis (Eqs. 1 and 2, Fig. 5). ΔE_Q for **Hox-CO** was similar to the value (~0.7 mms^{-1}) from Mössbauer data [55, 81] (Table 4). The larger Γ from NFS may result from the lower temperature (~50 K) in NFS vs. Mössbauer (~160 K) measurements. The ~25 % decrease of ΔE_Q and slight Γ decrease for **Hox-CO** vs. **Hox** likely reflected two more similar (octahedral) iron ions in [2Fe]. **Hox-O_2** as well showed a ~25 % diminished ΔE_Q and pronouncedly increased Γ vs. **Hox**, suggesting that Fe_p and Fe_d differed significantly in oxidation levels and one iron ion was more oxidized. The slightly diminished ΔE_Q of **HhydH**, which was similar to the Mössbauer value (Table 4) [42], and the more pronouncedly diminished Γ may be attributed to two more similar and more oxidized [2Fe] iron ions compared to **Hox**.

Valence level structure. The XANES pre-edge absorption probes resonant 1s electron excitation into unoccupied molecular orbitals (MOs) with valence character (core-to-valence transitions, ctv). The non-resonantly excited Kβ satellite emission probes electronic decay

from occupied valence levels to the core hole (valence-to-core transitions, vtc) of the whole H-cluster. The Kβ emission is split into $K\beta_{1,3}$ and Kβ′ features due to 3p/3d electron coupling (Fig. 2) and the Kβ′ line gains intensity for increasing unpaired Fe(3d) spin counts [66, 82-84], which facilitates monitoring of ctv transitions of low-spin iron in [2Fe] for Kβ′-detection or of high-spin iron in [4Fe4S] for $K\beta_{1,3}$-detection [36, 37]. Site-selective ctv spectra and vtc spectra for **Hox**, **Hox-O_2**, and **HhydH** are shown in Fig. 6A. The $K\beta_{1,3}$-detected ctv resembled the Kα-detected spectra (Fig. 2A) due to [4Fe4S] dominance whereas lower amplitudes and line shape/energy differences in the Kβ′-detected ctv revealed [2Fe] dominance. The ctv of **Hox-O_2** differed from **Hox** by a shift to higher energies for $K\beta_{1,3}$ detection and decreased lower-energy intensity for Kβ′ detection. The vtc showed a $K\beta_{2,5}$ energy up-shift and a Kβ′′ intensity gain. The ctv of **HhydH** was at lower energies for $K\beta_{1,3}$ detection and showed smaller lower-energy intensities as **Hox-O_2** for Kβ′ detection. The vtc showed a $K\beta_{2,5}$ energy down-shift and diminished lower-energy intensities vs. **Hox** (Fig. 6A).

Calculated ctv and vtc spectra are depicted in Fig. 6B. Globally similar ctv shapes and conservative spectral differences for **Hox**, **Hox-O_2**, and **HhydH** were obtained by DFT or time-dependent DFT (TDDFT) on small H-cluster models or on QM/MM structures (Fig. S10). DFT (TPSSh) on small models provided ctv/vtc spectra in good agreement with the experiment (Figs. 6B). The **Hox** and **Hox-O_2** structures well reproduced absolute shapes and relative differences in the experimental ctv of [4Fe4S] and [2Fe] and vtc of the whole H-cluster. Transitions involving unoccupied and occupied valence MOs thus were adequately described. For **Hox**, the α and β LUMOs were on [4Fe4S] whereas the α HOMO was mainly on Fe_d and the β HOMO on [4Fe4S].[37] The low-energy ctv peak of [2Fe] was dominated by excitation into MOs with Fe_d(3d)-character and the higher-energy peak by excitation into MOs with larger Fe_p and CO/CN^- characters (Fig. 6C). For **Hox-O_2**, the α and β LUMOs mostly on [2Fe] showed more equal Fe_p and Fe_d contributions and significant delocalization

onto the O_2^- ligand. Both HOMOs were mostly on [4Fe4S]. The ctv differences of [2Fe] were explained by enhanced transitions into the α LUMO, diminished lower-energy transitions into Fe_d-centered MOs and energy up-shifts and enhancement of transitions into MOs with Fe_p and/or Fe_d and CO/CN^- characters (Fig. 6C). The weak low-energy vtc increase for **Hox-O_2** reflected decay transitions from O(2s) dominated MOs. Notably, calculated ctv/vtc spectra for **Hox-CO** were similar for an apical CO or CN^- ligand at Fe_d [20, 37] (Fig. S10).

Calculated ctv spectra of [2Fe] and vtc spectra for structures with an apical hydride at Fe_d, with or without a proton at [4Fe4S], reproduced the **HhydH - Hox** spectral changes reasonably well (Figs. 6B, S10, S11). Protonation at [4Fe4S] has only a minor influence on the unoccupied MOs on [2Fe] and on the respective $K\beta_{2,5}$ emission. However, the ctv of **HhydH** revealed differences depending on which S-atom was protonated. For a proton at μS6, increased intensity in particular at higher ctv energies (~7115 eV) was observed whereas for a proton at S9(cys), the smaller intensity increase was in better agreement with the experimental **HhydH** – **Hox** difference (Figs. 6B, S11). For **HhydH**, LUMOs and HOMOs were largely on [4Fe4S]. The ctv differences of [2Fe] vs. **Hox** were mostly due to enhanced transitions into the LUMOs and into MOs with mixed [2Fe]/[4Fe4S] and hydride characters at low energies, as well as to up-shifted higher-energy transitions into MOs with enhanced delocalization over Fe_p/Fe_d and CO/CN^- (Fig. 6C, see Fig. S11 for further analysis).

Spin and charge distribution. Spin density (SD) and charge distributions at the H-cluster from DFT are shown in Figs. 7 and S13. For **Hox**, the unpaired spin mostly resided on Fe_d with few SD on the ligands and on [4Fe4S], corresponding to a mixed-valence [2Fe] site in a $[4Fe4S]^{2+}$-$[Fe_p^{2+}Fe_d^{1+}]$ complex (Fig. 7A,D). Fe_p and Fe_d carried similar positive charges, the [4Fe4S] core and adt/CO groups comparable negative charges, while most of the negative charge was located on CN^- and cysteine ligands (Fig. 7B). The mean α and β HOMO and

LUMO energies were ~2 eV and ~3.5 eV (LUMO – HOMO gap of ~1.5 eV) (Fig. 7C). For **Hox-CO**, increased SD at Fe_p and μCO led to a valence-delocalized [2Fe] site in a $[4Fe4S]^{2+}$-$[Fe_p^{1.5+}Fe_d^{1.5+}(CO^0)]$ complex (for an apical CO or CN^- at Fe_d) (Figs. 7A,C; S13) The HOMO was at similar energy as in **Hox**, the LUMO at ~0.5 eV higher energy, and the gap increased to ~2 eV in **Hox-CO** with an apical CN^-. For **Hox-O_2**, we found close to one spin on the O_2^- and very few SD on iron. Furthermore, a slight spin polarization with negative/positive SD on Fe_p/Fe_d and [4Fe4S]/cysteine, as well as increased positive charge on Fe_d and large negative charge on the superoxide were observed. A valence-localized $[4Fe4S]^{2+}$-$[Fe_p^{1+}Fe_d^{3+}(O_2^{1-})]$ complex with anti-ferromagnetic coupling of the low-spin ions in [2Fe] and an unpaired O(2p) spin in the π^* MO is a reasonable description of **Hox-O_2**. A similar HOMO energy as in **Hox** and a ~0.5 eV increased LUMO energy resulted in a larger gap (~2 eV) in **Hox-O_2**. For **HhydH** (proton at S9), almost one spin on the [4Fe4S] core, decreased SD on cysteines, and negligible spin on the hydride were found (Figs. 7A,D; S13), as well as less positive charge on Fe_d vs. Fe_p and diminished negative charge on cysteines vs. **Hox** (Fig. 7B). The proton at Fe_d carried few charge and thus exhibits weak hydride character. These results suggested a valence-delocalized [2Fe] in a $[(H^0)4Fe4S]^{1+}$-$[Fe_p^{2+}Fe_d^{2+}(H^0)]$ complex in **HhydH**. For the hydride state without a surplus proton, ~3 eV increased HOMO/LUMO energies vs. **Hox** were observed, whereas **HhydH** showed strongly diminished HOMO/LUMO energies, which were only ~0.5 eV larger than in **Hox** (Fig. 7C).

Structural models. H-cluster structures as suggested by our analyses are shown in Fig. 8 (for coordinates see Table S1). **Hox** features a distorted square-pyramidal Fe_d with an apical vacancy, a Fe_p-Fe_d distance of ~2.53 Å, a ~0.15 Å longer Fe_p-μCO than Fe_d-μCO bond, and a mean Fe-Fe distance of ~2.73 Å in [4Fe4S]. **Hox-CO** shows a near-octahedral Fe_d site, an elongated Fe_p-Fe_d distance (~2.67 Å) [85], more asymmetric μCO binding with a ~0.25 Å shorter Fe_p-μCO than Fe_d-μCO bond, a similar mean Fe-Fe distance in [4Fe4S] as **Hox**, a

slightly shorter Fe_d-CN^- than Fe_p-CN^- bond, and weak H-bonding of the apical CN^- to the adt group. **Hox-O_2** shows an apical O_2^- at a near-octahedral Fe_d, a slightly elongated Fe_p-Fe_d distance (~2.54 Å) vs. **Hox**, more symmetric μCO binding with a slightly shorter Fe_p-μCO bond, a similar mean Fe-Fe distance in [4Fe4S], and stronger H-bonding of the Fe_d-bound O-atom to the adt group. **HhydH** with a proton at S9 exhibits a Fe_d-H bond length of ~1.5 Å at a near-octahedral Fe_d, a slightly shortened Fe_p-Fe_d distance (~2.51 Å), less asymmetric μCO binding with a longer Fe_p-μCO bond, and a slightly increased mean Fe-Fe distance in [4Fe4S] vs. **Hox**, as well as a hydride-N(adt) distance of ~2.1 Å (for further structures see Fig. S14).

Discussion

Site-selective spectroscopy and quantum chemical theory has provided a consistent description of molecular and electronic structures, as well as of vibrational dynamics of H-cluster species in [FeFe]-hydrogenase HYDA1. **Hox** includes a μCO ligand and a square-pyramidal Fe_d with an apical vacancy, in agreement with crystal structures [16]. However, ligand binding in concert with protein dynamics may result in altered diiron site geometries [5, 32, 33]. The present data corroborate ligand rotation in **Hox-CO**, leading to an apical CN^- at Fe_d due to CO binding [20]. These findings and our computations imply that hydrogen-bonding to the distal CN^- is not decisive for the Fe_d geometry [86], but negatively charged ligands may be stabilized in apical position by weak H-bonding to the adt group. Our and earlier data [18, 87, 88] suggest that **Hox** corresponds to a mixed-valence $[4Fe4S]^{2+}$-$[Fe_p^{2+}Fe_d^{1+}]^{3-}$ complex whereas **Hox-CO** is best described as a valence-delocalized $[4Fe4S]^{2+}$-$[Fe_p^{1.5+}Fe_d^{1.5+}(CO)]^{3-}$ complex.

In C169A, a new H-cluster species (**Hox-O_2**) with the same redox level as **Hox** and an apical superoxide (O_2^-) at Fe_d accumulated at ambient O_2 pressure. A hydro-peroxo (OOH^-) ligand was excluded. **Hox-O_2** may be better described as a $[4Fe4S]^{2+}$-$[Fe_p^{1+}Fe_d^{3+}(O_2^{1-})]^{3-}$ complex than as a complex with a valence-delocalized diiron site. **Hox-O_2** was stable in

C169A protein in solution whereas similar O_2 exposure causes rapid H-cluster degradation in WT HYDA1 [6, 21]. Earlier studies have suggested initial O_2^- binding at [2Fe] also in WT, followed by structural degradation [21], as visible in crystal structures [16, 23]. Dehydrated [FeFe]-hydrogenases are completely resistant against O_2-induced H-cluster degradation [24]. These findings suggest that O_2^- protonation is required to form reactive oxygen species (ROS) for H-cluster degradation. When protonation is impaired due to interruption of the proton path to the active site in C169A or by depletion of adjacent water molecules, a bound O_2^- is stabilized and formation of mobile ROS is prevented. Accordingly, the conserved cysteine is essential as a proton transfer relay during O_2-induced inactivation of the H-cluster.

Under H_2, C169A adopted an H-cluster species (here denoted **HhydH**) that has been earlier described in WT, C169S, and μ-odt ($(SCH_2)_2O$) HYDA1 variants (and denoted "**Hhyd**") [29, 30, 35, 40, 42]. We assign it as a two-electron reduced structure with a μCO ligand and an apical hydride at Fe_d, in agreement with previous studies [35, 40, 42]. In addition, our experimental and computational data favor for **HhydH** a protonation at the sulfur atom of a terminal cysteine ligand at [4Fe4S]. We have recently proposed a similar protonation at [4Fe4S] for the one-electron reduced **Hred´** state, which also shows reduction of [4Fe4S] [29] **HhydH** is assigned to a $[(H)4Fe4S]^{1+}$-$[Fe_p^{2+}Fe_d^{2+}(H)]^{3-}$ complex with the net spin on the cubane. Under H_2 in the absence of (external) electron acceptors, **HhydH** accumulates pH-independently in C169A, C169S, and in the μ-odt ($(SCH_2)_2O$) derivative ($HydA1^{odt}$), while in WT ($HydA1^{adt}$) it accumulates at acidic pH [29, 30, 35, 40, 42] These findings suggest that after two-electron reduction of **Hox**, the hydride at [2Fe] in **HhydH** is trapped due to slowed or impaired proton release via the adt/C169 pathway whereas the protonation at [4Fe4S] is a consequence of the reduction of the cubane cluster [29]. If the proton at [4Fe4S] in **HhydH** stems from H_2, it may be delivered from the active site via a proton path including for example the bridging cysteine.

HhydH (earlier denoted "**Hhyd**") has been considered as an intermediate in H_2 conversion [29, 30, 35, 40, 42]. It shows a [2Fe] geometry with a μCO similar to **Hox** and **Hred´**, as opposed to a configuration lacking a μCO in **Hred** and **Hsred** [29, 39, 40]. **Hox** is converted to **Hred´** by a one-electron reduction step and a protonation at [4Fe4S] [29, 39]. That **Hred´** formation thus is charge-neutral may facilitate the second reduction step at a similar redox potential. Under H_2 formation conditions, **HhydH** therefore is accessible by one-electron reduction of **Hred´** and protonation at [2Fe] via the adt/C169 path. A second protonation at [2Fe] or delivery even of two protons to [2Fe] and subsequent deprotonation of [4Fe4S], leading to H_2 release, then may regain **Hox** (Fig. 9). More rapid protonation at [4Fe4S] (via adjacent water molecules as visible in all [FeFe]-hydrogenase structures [29]) than at [2Fe] during the first reduction by the physiological one-electron donors (cytochrome PetF in HYDA1 or accessory iron-sulfur clusters in bacterial enzymes) may localize the electron at [4Fe4S]. This sequence may prevent premature diiron site reduction, which leads to ligand rotation and μH binding. The resulting stabilization of a canonical cofactor geometry seems to be a prerequisite for continued H_2 formation in [FeFe]-hydrogenases.

Acknowledgments

M.H. thanks the Bundesministerium für Bildung und Forschung for funding (Grant 05K14KE1). T.H. thanks the Volkswagen Foundation for funding (Grant LigH2t) and the Deutsche Forschungsgemeinschaft (DFG) fur support within the Cluster of Excellence RESOLV (EXC1069). M. S. and S. T. S. thank the International Max Planck Research School (IMPRS) on Multiscale Biosystems and the Focus Area NanoScale (FU-Berlin) for financial support. U.-P.A. acknowledges funding by the Fonds der Chemischen Industrie (Liebig Grant) and the DFG (Emmy Noether Grant AP242/2-1). We thank the teams of P. Glatzel (ID26) and R. Rüffer (ID18) at ESRF for assistance and P. Chernev (FU-Berlin) for data analysis software.

Supporting Information Available

Model structures for DFT and QM/MM, FTIR spectra of HYDA1, calculation of IR spectra of **Hox**, calculated IR spectra of **Hox-O_2** species, experimental and calculated IR spectra of **Hsred**, calculated IR spectra for varying protonation sites, NRVS spectra of **Hox-CO** with varying ^{57}Fe labeling, calculated NRVS spectra from DFT and QM/MM, hydride vibrations in **HhydH**, ctv and vtc spectra from DFT, TDDFT, and QM/MM, further ctv and vtc analysis, molecular (frontier) orbitals from DFT, spin distribution in further H-cluster species, structures of further H-cluster species from DFT, coordinates of H-cluster structures.

References

[1] J. Rifkin, The Hydrogen Economy, Tarcher Penguin, New York, 2002.
[2] R.F. Cammack, M.; Robson, R., Hydrogen as a fuel: Learning from Nature., in, Taylor & Francis, London, UK, 1997.
[3] M. Rakowski DuBois, D.L. DuBois, The roles of the first and second coordination spheres in the design of molecular catalysts for H2 production and oxidation, Chem. Soc. Rev. 38 (2009) 62-72.
[4] T.R. Simmons, G. Berggren, M. Bacchia, M. Fontecave, V. Artero, Mimicking hydrogenases: from biomimetics to artificial enzymes, Coord. Chem. Rev. 270-271 (2014) 127-150.
[5] W. Lubitz, H. Ogata, O. Rudiger, E. Reijerse, Hydrogenases, Chem. Rev. 114 (2014) 4081-4148.
[6] S.T. Stripp, T. Happe, How algae produce hydrogen - news from the photosynthetic hydrogenase, Dalton Trans. (2009) 9960-9969.
[7] M. Winkler, J. Esselborn, T. Happe, Molecular basis of [FeFe]-hydrogenase function: An insight into the complex interplay between protein and catalytic cofactor, Biochim. Biophys. Acta 1827 (2013) 974-985.
[8] V. Artero, G. Berggren, M. Atta, G. Caserta, S. Roy, L. Pecqueur, M. Fontecave, From enzyme maturation to synthetic chemistry: the case of hydrogenases, Acc. Chem. Res. 48 (2015) 2380-2387.
[9] F. Gloaguen, T.B. Rauchfuss, Small molecule mimics of hydrogenases: hydrides and redox, Chem. Soc. Rev. 38 (2009) 100-108.
[10] M.Y. Darensbourg, R.D. Bethel, Biomimetic chemistry - merging the old with the new, Nat. Chem. 4 (2012) 11-13.
[11] C. Tard, C.J. Pickett, Structural and functional analogues of the active sites of the [Fe]-, [NiFe]-, and [FeFe]-hydrogenases, Chem. Rev. 109 (2009) 2245-2274.
[12] T. Happe, A. Hemschemeier, Metalloprotein mimics - old tools in a new light, Trends Biotechnol. 32 (2014) 170-176.
[13] S. Poudel, M. Tokmina-Lukaszewska, D.R. Colman, M. Refai, G.J. Schut, P.W. King, P.C. Maness, M.W.W. Adams, J.W. Peters, B. Bothner, E.S. Boyd, Unification of [FeFe]-hydrogenases into three structural and functional groups, Biochim. Biophys. Acta 1860 (2016) 1910-1921.
[14] J.W. Peters, W.N. Lanzilotta, B.J. Lemon, L.C. Seefeldt, X-ray crystal structure of the Fe-only hydrogenase (CpI) from *Clostridium pasteurianum* to 1.8 angstrom resolution, Science 282 (1998) 1853-1858.
[15] Y. Nicolet, B.J. Lemon, J.C. Fontecilla-Camps, J.W. Peters, A novel FeS cluster in Fe-only hydrogenases, Trends Biochem. Sci. 25 (2000) 138-143.
[16] J. Esselborn, N. Muraki, K. Klein, V. Engelbrecht, N. Metzler-Nolte, U.-P. Apfel, E. Hofmann, G. Kurisu, T. Happe, A structural view of synthetic cofactor integration into [FeFe]-hydrogenases, Chem. Sci. 7 (2016) 959-968
[17] A.J. Pierik, M. Hulstein, W.R. Hagen, S.P. Albracht, A low-spin iron with CN and CO as intrinsic ligands forms the core of the active site in [Fe]-hydrogenases, Eur. J. Biochem. 258 (1998) 572-578.
[18] A. Silakov, B. Wenk, E. Reijerse, W. Lubitz, (14)N HYSCORE investigation of the H-cluster of [FeFe] hydrogenase: evidence for a nitrogen in the dithiol bridge, Phys. Chem. Chem. Phys. 11 (2009) 6592-6599.
[19] W. Roseboom, A.L. De Lacey, V.M. Fernandez, E.C. Hatchikian, S.P. Albracht, The active site of the [FeFe]-hydrogenase from *Desulfovibrio desulfuricans*. II. Redox properties, light sensitivity and CO-ligand exchange as observed by infrared spectroscopy, J. Biol. Inorg. Chem. 11 (2006) 102-118.

[20] M. Senger, S. Mebs, J. Duan, F. Wittkamp, U.P. Apfel, J. Heberle, M. Haumann, S.T. Stripp, Stepwise isotope editing of [FeFe]-hydrogenases exposes cofactor dynamics, Proc. Natl. Acad. Sci. U. S. A. 113 (2016) 8454–8459.
[21] C. Lambertz, N. Leidel, K.G. Havelius, J. Noth, P. Chernev, M. Winkler, T. Happe, M. Haumann, O2 reactions at the six-iron active site (H-cluster) in [FeFe]-hydrogenase, J. Biol. Chem. 286 (2011) 40614-40623.
[22] S.T. Stripp, G. Goldet, C. Brandmayr, O. Sanganas, K.A. Vincent, M. Haumann, F.A. Armstrong, T. Happe, How oxygen attacks [FeFe] hydrogenases from photosynthetic organisms, Proc. Natl. Acad. Sci. U. S. A. 106 (2009) 17331-17336.
[23] K.D. Swanson, M.W. Ratzloff, D.W. Mulder, J.H. Artz, S. Ghose, A. Hoffman, S. White, O.A. Zadvornyy, J.B. Broderick, B. Bothner, P.W. King, J.W. Peters, [FeFe]-hydrogenase oxygen inactivation is initiated at the H cluster 2Fe subcluster, J. Am. Chem. Soc. 137 (2015) 1809-1816.
[24] J. Noth, R. Kositzki, K. Klein, M. Winkler, M. Haumann, T. Happe, Lyophilisation protects [FeFe]-hydrogenases against O2-induced H-cluster inactivation, Nat. Sci. Rep. 5 (2015) 1-10.
[25] A.A. Oughli, F. Conzuelo, M. Winkler, T. Happe, W. Lubitz, W. Schuhmann, O. Rudiger, N. Plumere, A redox hydrogel protects the O2 -sensitive [FeFe]-hydrogenase from Chlamydomonas reinhardtii from oxidative damage, Angew. Chem. Int. Ed. Engl. 54 (2015) 12329-12333.
[26] F.A. Armstrong, R.M. Evans, S.V. Hexter, B.J. Murphy, M.M. Roessler, P. Wulff, Guiding principles of hydrogenase catalysis instigated and clarified by protein film electrochemistry, Acc. Chem. Res. 49 (2016) 884-892.
[27] A. Kubas, C. Orain, D. De Sancho, L. Saujet, M. Sensi, C. Gauquelin, I. Meynial-Salles, P. Soucaille, H. Bottin, C. Baffert, V. Fourmond, R.B. Best, J. Blumberger, C. Léger, Mechanism of O2 diffusion and reduction in FeFe hydrogenases, Nat. Chem. 9 (2017) 88–95.
[28] C. Orain, L. Saujet, C. Gauquelin, P. Soucaille, I. Meynial-Salles, C. Baffert, V. Fourmond, H. Bottin, C. Leger, Electrochemical measurements of the kinetics of inhibition of two FeFe hydrogenases by O2 demonstrate that the reaction is partly reversible, J. Am. Chem. Soc. 137 (2015) 12580-12587.
[29] M. Senger, S. Mebs, J. Duan, O. Shulenina, K. Laun, L. Kertess, F. Wittkamp, U.-P. Apfel, T. Happe, M. Winkler, M. Haumann, S.T. Stripp, Protonation and reduction dynamics at the hydrogen-forming cofactor of [FeFe]-hydrogenases, Chem. Sci., under revision (2017).
[30] D.W. Mulder, M.W. Ratzloff, M. Bruschi, C. Greco, E. Koonce, J.W. Peters, P.W. King, Investigations on the role of proton-coupled electron transfer in hydrogen activation by [FeFe]-hydrogenase, J. Am. Chem. Soc. 136 (2014) 15394-15402.
[31] S. Morra, A. Giraudo, G. Di Nardo, P.W. King, G. Gilardi, F. Valetti, Site saturation mutagenesis demonstrates a central role for cysteine 298 as proton donor to the catalytic site in CaHydA [FeFe]-hydrogenase, PloSone 7 (2012) e48400.
[32] P. Knorzer, A. Silakov, C.E. Foster, F.A. Armstrong, W. Lubitz, T. Happe, Importance of the protein framework for catalytic activity of [FeFe]-hydrogenases, J. Biol. Chem. 287 (2012) 1489-1499.
[33] V. Fourmond, C. Greco, K. Sybirna, C. Baffert, P.H. Wang, P. Ezanno, M. Montefiori, M. Bruschi, I. Meynial-Salles, P. Soucaille, J. Blumberger, H. Bottin, L. De Gioia, C. Leger, The oxidative inactivation of FeFe hydrogenase reveals the flexibility of the H-cluster, Nat Chem. 6 (2014) 336-342.
[34] S. Katz, J. Noth, M. Horch, H.S. Shafaat, T. Happe, P. Hildebrandt, I. Zebger, Vibrational spectroscopy reveals the initial steps of biological hydrogen evolution, Chem. Sci. 7 (2016) 6746-6752.

[35] M. Winkler, M. Senger, J. Duan, J. Esselborn, F. Wittkamp, E. Hofmann, U.-P. Apfel, S.T. Stripp, T. Happe, Accumulating the hydride state in the catalytic cycle of [FeFe]-Hydrogenases, Nat. Commun., in press (2017).
[36] C. Lambertz, P. Chernev, K. Klingan, N. Leidel, K.G.V. Siegfridsson, T. Happe, M. Haumann, Electronic and molecular structures of the [2Fe] and [4Fe4S] units of the active-site H-cluster in [FeFe]-hydrogenase determined by spin- and site-selective XAE and DFT, Chem. Sci. 5 (2014) 1187-1203.
[37] P. Chernev, C. Lambertz, A. Brunje, N. Leidel, K.G. Sigfridsson, R. Kositzki, C.H. Hsieh, S. Yao, R. Schiwon, M. Driess, C. Limberg, T. Happe, M. Haumann, Hydride binding to the active site of [FeFe]-hydrogenase, Inorg. Chem. 53 (2014) 12164-12177.
[38] A. Adamska, A. Silakov, C. Lambertz, O. Rudiger, T. Happe, E. Reijerse, W. Lubitz, Identification and characterization of the "super-reduced" state of the H-cluster in [FeFe] hydrogenase: a new building block for the catalytic cycle?, Angew. Chem. Int. Ed. Engl. 51 (2012) 11458-11462.
[39] C. Sommer, A. Adamska-Venkatesh, K. Pawlak, J.A. Birrell, O. Rudiger, E.J. Reijerse, W. Lubitz, Proton coupled electronic rearrangement within the H-Cluster as an essential step in the catalytic cycle of [FeFe] hydrogenases, J. Am. Chem. Soc. 139 (2017) 1440-1443.
[40] E.J. Reijerse, C.C. Pham, V. Pelmenschikov, R. Gilbert-Wilson, A. Adamska-Venkatesh, J.F. Siebel, L.B. Gee, Y. Yoda, K. Tamasaku, W. Lubitz, T.B. Rauchfuss, S.P. Cramer, Direct observation of an iron-bound terminal hydride in [FeFe]-hydrogenase by nuclear resonance vibrational spectroscopy, J. Am. Chem. Soc. 139 (2017) 4306-4309.
[41] A. Adamska-Venkatesh, D. Krawietz, J. Siebel, K. Weber, T. Happe, E. Reijerse, W. Lubitz, New redox states observed in [FeFe] hydrogenases reveal redox coupling within the H-cluster, J. Am. Chem. Soc. 136 (2014) 11339-11346.
[42] D.W. Mulder, Y. Guo, M.W. Ratzloff, P.W. King, Identification of a catalytic iron-hydride at the H-cluster of [FeFe]-hydrogenase, J. Am. Chem. Soc. 139 (2016) 83–86.
[43] D.W. Mulder, M.W. Ratzloff, E.M. Shepard, A.S. Byer, S.M. Noone, J.W. Peters, J.B. Broderick, P.W. King, EPR and FTIR analysis of the mechanism of H2 activation by [FeFe]-hydrogenase HydA1 from *Chlamydomonas reinhardtii*, J. Am. Chem. Soc. 135 (2013) 6921-6929.
[44] S. Hugenbruch, H.S. Shafaat, T. Kramer, M.U. Delgado-Jaime, K. Weber, F. Neese, W. Lubitz, S. DeBeer, In search of metal hydrides: an X-ray absorption and emission study of [NiFe] hydrogenase model complexes, Phys. Chem. Chem. Phys. 18 (2016) 10688-10699.
[45] H.S. Shafaat, O. Rudiger, H. Ogata, W. Lubitz, [NiFe] hydrogenases: A common active site for hydrogen metabolism under diverse conditions, Biochim. Biophys. Acta 1827 (2013) 986-1002.
[46] H.S. Shafaat, K. Weber, T. Petrenko, F. Neese, W. Lubitz, Key hydride vibrational modes in [NiFe] hydrogenase model compounds studied by resonance Raman spectroscopy and density functional calculations, Inorg. Chem. 51 (2012) 11787-11797.
[47] H. Ogata, T. Kramer, H.X. Wang, D. Schilter, V. Pelmenschikov, M. van Gastel, F. Neese, T.B. Rauchfuss, L.B. Gee, A.D. Scott, Y. Yoda, Y. Tanaka, W. Lubitz, S.P. Cramer, Hydride bridge in [NiFe]-hydrogenase observed by nuclear resonance vibrational spectroscopy, Nat. Commun. 6 (2015).
[48] H. Ogata, K. Nishikawa, W. Lubitz, Hydrogens detected by subatomic resolution protein crystallography in a [NiFe] hydrogenase, Nature 520 (2015) 571-574.
[49] R. Gilbert-Wilson, J.F. Siebel, A. Adamska-Venkatesh, C.C. Pham, E. Reijerse, H. Wang, S.P. Cramer, W. Lubitz, T.B. Rauchfuss, Spectroscopic investigations of [FeFe] hydrogenase maturated with [(57)Fe2(adt)(CN)2(CO)4](2.), J. Am. Chem. Soc. 137 (2015) 8998-9005.

[50] A. Adamska-Venkatesh, T.R. Simmons, J.F. Siebel, V. Artero, M. Fontecave, E. Reijerse, W. Lubitz, Artificially maturated [FeFe] hydrogenase from *Chlamydomonas reinhardtii*: a HYSCORE and ENDOR study of a non-natural H-cluster, Phys. Chem. Chem. Phys. 17 (2015) 5421-5430.
[51] A. Adamska-Venkatesh, S. Roy, J.F. Siebel, T.R. Simmons, M. Fontecave, V. Artero, E. Reijerse, W. Lubitz, Spectroscopic characterization of the bridging amine in the active site of [FeFe] hydrogenase using isotopologues of the H-cluster, J. Am. Chem. Soc. 137 (2015) 12744-12747.
[52] J. Esselborn, C. Lambertz, A. Adamska-Venkatesh, T. Simmons, G. Berggren, J. Noth, J. Siebel, A. Hemschemeier, V. Artero, E. Reijerse, M. Fontecave, W. Lubitz, T. Happe, Spontaneous activation of [FeFe]-hydrogenases by an inorganic [2Fe] active site mimic, Nat. Chem. Biol. 10 (2013) 607-609.
[53] G. Berggren, A. Adamska, C. Lambertz, T.R. Simmons, J. Esselborn, M. Atta, S. Gambarelli, J.M. Mouesca, E. Reijerse, W. Lubitz, T. Happe, V. Artero, M. Fontecave, Biomimetic assembly and activation of [FeFe]-hydrogenases, Nature 499 (2013) 66-69.
[54] J. Noth, J. Esselborn, J. Guldenhaupt, A. Brunje, A. Sawyer, U.P. Apfel, K. Gerwert, E. Hofmann, M. Winkler, T. Happe, [FeFe]-Hydrogenase with chalcogenide substitutions at the H-Cluster maintains full H-2 evolution activity, Angew. Chem. Int. Ed. Engl. 55 (2016) 8396-8400.
[55] R. Gilbert-Wilson, J.F. Siebel, A. Adamska-Venkatesh, C.C. Pham, E. Reijerse, H. Wang, S.P. Cramer, W. Lubitz, T.B. Rauchfuss, Spectroscopic investigations of [FeFe] hydrogenase maturated with [(57)Fe2(adt)(CN)2(CO)4](2-), J. Am. Chem. Soc. 137 (2015) 8998-9005.
[56] B. Moeser, A. Janoschka, J.A. Wolny, H. Paulsen, I. Filippov, R.E. Berry, H. Zhang, A.I. Chumakov, F.A. Walker, V. Schunemann, Nuclear inelastic scattering and Mössbauer spectroscopy as local probes for ligand binding modes and electronic properties in proteins: vibrational behavior of a ferriheme center inside a beta-barrel protein, J. Am. Chem. Soc. 134 (2012) 4216-4228.
[57] R. Kositzki, S. Mebs, J. Marx, J.J. Griese, N. Schuth, M. Högbom, V. Schünemann, M. Haumann, Protonation state of MnFe and FeFe cofactors in a ligand binding oxidase revealed by X ray absorption, emission, and vibrational spectroscopy and QM/MM calculations, Inorg. Chem. 19 (2016) 9869-9885.
[58] R. Rüffer, Nuclear Resonance Scattering, in: H. Saleem (Ed.) Reference Module in Materials Science and Materials Engineering, Elsevier, Amsterdam, 2016, pp. 1-13.
[59] W. Sturhahn, Nuclear resonant spectroscopy, J. Phys. Condens. Matt. 16 (2004) S497-S530.
[60] A.L. De Lacey, C. Stadler, C. Cavazza, E.C. Hatchikian, V.M. Fernandez, FTIR characterization of the active site of the Fe-hydrogenase from *Desulfovibrio desulfuricans*, J. Am. Chem. Soc. 122 (2000) 11232-11233.
[61] A. Silakov, C. Kamp, E. Reijerse, T. Happe, W. Lubitz, Spectroelectrochemical characterization of the active site of the [FeFe] hydrogenase HydA1 from *Chlamydomonas reinhardtii*, Biochemistry 48 (2009) 7780-7786.
[62] N. Leidel, C.H. Hsieh, P. Chernev, K.G. Sigfridsson, M.Y. Darensbourg, M. Haumann, Bridging-hydride influence on the electronic structure of an [FeFe] hydrogenase active-site model complex revealed by XAES-DFT, Dalton Trans. 42 (2013) 7539-7554.
[63] N. Leidel, P. Chernev, K.G. Havelius, S. Ezzaher, S. Ott, M. Haumann, Site-selective X-ray spectroscopy on an asymmetric model complex of the [FeFe] hydrogenase active site, Inorg. Chem. 51 (2012) 4546-4559.
[64] M.K. Akhtar, P.R. Jones, Deletion of iscR stimulates recombinant clostridial Fe-Fe hydrogenase activity and H2-accumulation in *Escherichia coli* BL21(DE3), Appl. Microbiol. Biotechnol. 78 (2008) 853-862.

[65] I. Zaharieva, P. Chernev, G. Berggren, M. Anderlund, S. Styring, H. Dau, M. Haumann, Room-temperature energy-sampling Kbeta X-ray emission spectroscopy of the Mn4Ca complex of photosynthesis reveals three manganese-centered oxidation steps and suggests a coordination change prior to O2 formation, Biochemistry 55 (2016) 4197-4211.
[66] M. Mebs, N. Braun, R. Kositzki, C. Limberg, M. Haumann, Abrupt versus gradual spin-crossover in Fe(II)(phen)2(NCS)2 and Fe(III)(dedtc)3 compared by X-ray absorption and emission spectroscopy and quantum-chemical calculations, Inorg Chem. 54 (2015) 11606-11624.
[67] S. Yao, F. Meier, N. Lindenmaier, R. Rudolph, B. Blom, M. Adelhardt, J. Sutter, S. Mebs, M. Haumann, K. Meyer, M. Kaupp, M. Driess, Biomimetic reduced [2Fe−2S] clusters with unprecedentedly delocalized mixed-valence iron centers, Angew. Chem. Int. Ed. Engl. 54 (2015) 12506-12510.
[68] A. Chumakov, R. Ruffer, Nuclear inelastic scattering, Hyperfine Interact. 113 (1998) 59-79.
[69] A.I. Chumakov, A.Q.R. Baron, R. Ruffer, H. Grunsteudel, H.F. Grunsteudel, A. Meyer, Nuclear resonance energy analysis of inelastic x-ray scattering, Phys. Rev. Lett. 76 (1996) 4258-4261.
[70] D.W. Mulder, E.S. Boyd, R. Sarma, R.K. Lange, J.A. Endrizzi, J.B. Broderick, J.W. Peters, Stepwise [FeFe]-hydrogenase H-cluster assembly revealed in the structure of HydA(DeltaEFG), Nature 465 (2010) 248-251.
[71] T. Vreven, K. Morokuma, O. Farkas, H.B. Schlegel, M.J. Frisch, Geometry optimization with QM/MM, ONIOM, and other combined methods. I. Microiterations and constraints, J. Comput. Chem. 24 (2003) 760-769.
[72] S. Dapprich, I. Komaromi, K.S. Byun, K. Morokuma, M.J. Frisch, A new ONIOM implementation in Gaussian98. Part I. The calculation of energies, gradients, vibrational frequencies and electric field derivatives, J. Mol. Struc. Theor. Chem. 461 (1999) 1-21.
[73] M.J.T. Frisch, G. W.; Schlegel, H. B.; Scuseria, G. E.; Robb, M. A.; Cheeseman, J. R.; Scalmani, G.; Barone, V.; Mennucci, B.; Petersson, G. A.; Nakatsuji, H.; Caricato, M.; Li, X.; Hratchian, H. P.; Izmaylov, A. F.; Bloino, J.; Zheng, G.; Sonnenberg, J. L.; Hada, M.; Ehara, M.; Toyota, K.; Fukuda, R.; Hasegawa, J.; Ishida, M.; Nakajima, T.; Honda, Y.; Kitao, O.; Nakai, H.; Vreven, T.; Montgomery, J. A., Jr.; Peralta, J. E.; Ogliaro, F.; Bearpark, M.; Heyd, J. J.; Brothers, E.; Kudin, K. N.; Staroverov, V. N.; Kobayashi, R.; Normand, J.; Raghavachari, K.; Rendell, A.; Burant, J. C.; Iyengar, S. S.; Tomasi, J.; Cossi, M.; Rega, N.; Millam, J. M.; Klene, M.; Knox, J. E.; Cross, J. B.; Bakken, V.; Adamo, C.; Jaramillo, J.; Gomperts, R.; Stratmann, R. E.; Yazyev, O.; Austin, A. J.; Cammi, R.; Pomelli, C.; Ochterski, J. W.; Martin, R. L.; Morokuma, K.; Zakrzewski, V. G.; Voth, G. A.; Salvador, P.; Dannenberg, J. J.; Dapprich, S.; Daniels, A. D.; Farkas, Ö.; Foresman, J. B.; Ortiz, J. V.; Cioslowski, J.; Fox, D. J. , Gaussian 09, Revision D.01., Gaussian, Inc., Wallingford CT (2009).
[74] A.D. Becke, Density-functional exchange-energy approximation with correct asymptotic behavior, Phys. Rev. A 38 (1988) 3098-3100.
[75] A. Schäfer, C. Huber, R. Ahlrichs, Fully optimized contracted Gaussian basis sets of triple zeta valence quality for atoms Li to Kr, J. Chem. Phys. 100 (1994) 5829-5835.
[76] C. Lee, W. Yang, R.G. Parr, Development of the Colle-Salvetti correlation-energy formula into a functional of the electron density, Phys. Rev. B Condens. Matt. 37 (1988) 785-789.
[77] M. Reiher, O. Salomon, B.A. Hess, Reparameterization of hybrid functionals based on energy differences of states of different multiplicity, Theor. Chem. Acc. 107 (2001) 48-55.

[78] H. Paulsen, H. Winkler, A.X. Trautwein, H. Grunsteudel, V. Rusanov, H. Toftlund, Measurement and simulation of nuclear inelastic-scattering spectra of molecular crystals, Phys. Rev. B 59 (1999) 975-984.
[79] F. Neese, The ORCA program system, Wires Comput. Mol. Sci. 2 (2012) 73-78.
[80] N. Leidel, P. Chernev, K.G. Havelius, L. Schwartz, S. Ott, M. Haumann, Electronic structure of an [FeFe] hydrogenase model complex in solution revealed by X-ray absorption spectroscopy using narrow-band emission detection, J. Am. Chem. Soc. 134 (2012) 14142-14157.
[81] A.S. Pereira, P. Tavares, I. Moura, J.J. Moura, B.H. Huynh, Mössbauer characterization of the iron-sulfur clusters in Desulfovibrio vulgaris hydrogenase, J. Am. Chem. Soc. 123 (2001) 2771-2782.
[82] C.J. Pollock, M.U. Delgado-Jaime, M. Atanasov, F. Neese, S. DeBeer, K beta mainline X-ray emission spectroscopy as an experimental probe of metal-ligand covalency, J. Am. Chem. Soc. 136 (2014) 9453-9463.
[83] P. Glatzel, L. Jacquamet, U. Bergmann, F.M.F. de Groot, S.P. Cramer, Site-selective EXAFS in mixed-valence compounds using high-resolution fluorescence detection: A study of iron in Prussian Blue, Inorg. Chem. 41 (2002) 3121-3127.
[84] G. Vankó, T. Neisius, M. G., F. Renz, S. Karpati, A. Shukla, F.M. de Groot, Probing the 3d spin momentum with X-ray emission spectroscopy: the case of molecular-spin transitions, J. Phys. Chem. B 110 (2006) 11647-11653.
[85] S. Stripp, O. Sanganas, T. Happe, M. Haumann, The structure of the active site H-cluster of [FeFe] hydrogenase from the green alga *Chlamydomonas reinhardtii* studied by X-ray absorption spectroscopy, Biochemistry 48 (2009) 5042-5049.
[86] A.R. Finkelmann, M.T. Stiebritz, M. Reiher, Inaccessibility of the μ-hydride species in [FeFe] hydrogenases, Chem. Sci. 5 (2014) 215-221.
[87] A. Silakov, B. Wenk, E. Reijerse, S.P. Albracht, W. Lubitz, Spin distribution of the H-cluster in the H(ox)-CO state of the [FeFe] hydrogenase from *Desulfovibrio desulfuricans*: HYSCORE and ENDOR study of (14)N and (13)C nuclear interactions, J Biol Inorg. Chem. 14 (2009) 301-313.
[88] A. Silakov, E.J. Reijerse, S.P. Albracht, E.C. Hatchikian, W. Lubitz, The electronic structure of the H-cluster in the [FeFe]-hydrogenase from *Desulfovibrio desulfuricans*: a Q-band 57Fe-ENDOR and HYSCORE study, J. Am. Chem. Soc. 129 (2007) 11447-11458.

Table 1: Fe K-edge and $K\beta_{1,3}$ emission line energies of the H-cluster.

			K-edge detection energy					
			Kα	$K\beta_{1,3}$	Kβ´	Kα	$K\beta_{1,3}$	Kβ´
variant	species	$E(K\beta_{1,3})$ [eV][a]	K-edge energy, E [eV][b]			$E_{Hi} - E_{Hox}$ [eV]		
WT	**Hox**	7058.49(5)	7119.7(1)	7119.6(1)	7120.8(1)	-	-	-
C169A	**Hox-O_2**	7058.62(5)	7120.3(1)	7119.8(1)	7121.7(1)	+0.6	+0.2	+0.9
	HhydH	7058.38(5)	7118.9(1)	7119.1(1)	7121.2(1)	-0.8	-0.6	+0.3

[a]Energies of non-resonantly excited Kβ spectra were determined from first-moment calculation in a 7052-7065 eV range [65], [b]energies were determined at K-edge half-height (50 %); energy errors in parenthesis.

Table 2: Infrared bands of CO and CN^- ligands.[a]

species	IR band	ligand	frequency, ν [cm^{-1}]	area, a [%]	$\nu_{Hi} - \nu_{Hox}$ (exp)	$\nu_{Hi} - \nu_{Hox}$ (cal)	$a_{Hi} - a_{Hox}$ (exp)	$a_{Hi} - a_{Hox}$ (cal)
Hox	α	CO	1804	16	-	-	-	-
	β		1940	50	-	-	-	-
	γ		1964	17	-	-	-	-
	ε	CN^-	2073	9	-	-	-	-
	ζ		2088	8	-	-	-	-
HhydH	α	CO	1863	14	+59	+62 [+20]	-2	+1
	β		1962	41	+22	+24 [-18]	-9	-13
	γ		1978	26	+13	+5 [-15]	+9	+9
	ε	CN^-	2076	9	+4	+8 [-9]	0	+1
	ζ		2087	10	-1	+6 [-8]	+2	+2
Hox-O_2	α	CO	1863	20	+59	+62	+4	+5
	β		1991	41	+51	+54	-9	-9
	γ		2007	19	+43	+37	+2	+3
	ε	CN^-	2089	10	+16	+21	+1	0
	ζ		2100	10	+12	+17	+2	+1
Hox-CO	α	CO	1809	21	+5	-4	+5	+7
	β		1963	15	+23	+24	-35	-44
	γ		1969	19	+5	+3	+2	+6
	δ		2013	27	-	-	-	-
	ε	CN^-	2082	8	+10	+14	-1	-1
	ζ		2091	10	+3	+11	+2	0

[a]Experimental (rounded) frequencies and (normalized) intensities of CO and CN^- ligand bands correspond to FTIR spectra in Fig. 3. Calculated frequency and intensity differences represent mean values for IR data from DFT and QM/MM (ONIOM) calculations (at BP86 or TPSSh levels). **Hox-CO** carries an apical CN^- at Fe_d; **HhydH** denotes a double-reduced species with a proton at [4Fe4S] (at S9) and an apical proton at Fe_d (values for a structure without [4Fe4S] protonation in brackets).

Table 3: Correlation between calculated and experimental IR frequencies.[a]

H-cluster species	rmsd [cm^{-1}]
Hox	8
Hox-O_2	10
Hox-O_2H	27
Hox-CO (aCO)	22
Hox-CO (aCN)	11
"Hhyd" (aH, eCN)	19
"Hhyd" (eH, aCN)	33
HhydH (aH, NadtH)	25
HhydH (eH, NadtH)	31
HhydH (aH, eCN, S1/2H)	21
HhydH (eH, aCN, S1/2H)	29
HhydH (aH, eCN, S6H)	10
HhydH (eH, aCN, S6H)	23
HhydH (aH, eCN, S9H)	10
HhydH (eH, aCN, S9H)	16

[a]rmsd values were calculated for IR frequencies (F^{cal}) of CO/CN^- ligands of species from TPSSh, BP86, TPSSh/ONIOM, and BP86/ONIOM approaches using Eq. 3 and F^{cal} correction as described in Fig. 3. Values of rmsd from the four theory levels were normalized so that the respective rmsd for **Hox** was equal to the rmsd of **Hox** from DFT/TPSSh and thereafter, rmsd values were averaged for each species (non-normalized mean rmsd for **Hox** 12±4 cm^{-1}, mean standard deviation of normalized rmsd values of the other species ~6 cm^{-1}). Annotations (a) and (e) denote ligands in apical or equatorial position at Fe_d, for S-atom numbering see Fig. 1B, H means addition of a proton at respective positions, e.g. addition of a second proton at NH(adt). Note that absolute rmsd levels varied by a factor of ~2 between theory levels, but similar relative rmsd changes were observed for all approaches.

Table 4: Nuclear quadrupole splitting energy and Mössbauer linewidth from NFS.[a]

variant	H-cluster	ΔE_Q [mms^{-1}]	Γ [mms^{-1}]
WT	**Hox**	1.01	0.63
	Hox-CO	0.78 (0.71±0.17)	0.57
C169A	**Hox-O_2**	0.79	0.80
	HhydH	0.88 (0.87±0.19)	0.42

[a]The error of ΔE_Q and Γ from NFS is ~0.05 mms^{-1}, mean ΔE_Q values for **HhydH** and **Hox-CO** from Mössbauer spectroscopy in parenthesis (±full range for the two iron ions in [2Fe]) [42, 55, 81].

Legends to Figures

Figure 1: The H-cluster in [FeFe]-hydrogenase. (A) Cofactor with [4Fe4S] and [2Fe] sub-complexes in a crystal structure of oxidized CPI enzyme from *C. pasteurianum* (PDB entry 4XDC, 1.63 Å resolution) [16]. Fe_p and Fe_d denote iron ions in [2Fe], the blue circle marks the vacancy at Fe_d, W_i denotes water molecules, magenta dashes show putative H-bonding interactions. The amino acid numbering is for CPI, Cys299 corresponds to Cys169 and Ser232 to an alanine in HYDA1. (B) Schematic H-cluster structure for **Hox**, highlighting CO/CN^- ligands and the adt bridge at [2Fe] (sulfur atoms are numbered 1-10).

Figure 2: Fe K-edge absorption and Kβ emission spectra of HYDA1. (A) Main panel: XANES spectra of WT (**Hox**, **Hox-CO**) and C169A (**Hox-O_2**, **HhydH**) for broad-band Kα emission detection. Inset: XANES spectra for narrow-band Kβ emission detection at indicated energies (spectra smoothed over data points within 2.5 eV for clarity). (B) Main panel: Kβ main-line emission spectra and difference spectra (x5). Inset: magnified $K\beta_{1,3}$ region.

Figure 3: Experimental and calculated infrared spectra. (A) Experimental FTIR spectra (black lines) of main H-cluster species in WT and C169A HydA1 (see Fig. S2) and simulation curves (colored lines) with frequencies/intensities of CO (α, β, γ, δ) and CN^- (ζ, ε) bands in Table 2. (B) Calculated spectra from DFT (TPSSh, small models; Fig. S1) for **Hox**, **Hox-CO** (aCO/CN = apical CO or CN^- at Fe_d), **Hox-O_2**, and for the hydride state with only an apical proton at Fe_d (**Hhyd**) or an additional proton at S9 of [4Fe4S] (**HhydH**). Stick spectra were broadened with experimental band widths and shifted by -39 cm^{-1} (CN^- bands 2-fold magnified). (C) Correlation of calculated and experimental IR frequencies (F) and intensities (inset). Straight lines show fits to **Hox** data (F_{Hox}^{cal} = -266±97 cm^{-1} + 1.16±0.05 x F_{Hox}^{exp},

$rmsd_F$ for all species (i) was derived using $F_i^{cor} = (F_i^{cal} + 266\ cm^{-1}) / 1.16$ in Eq. 3) [29]. (D) Calculated vibrational modes (arrows, vibrational amplitudes/directions; not drawn to scale).

Figure 4: Nuclear resonance vibrational spectroscopy on the H-cluster. Top: experimental PDOS spectra from NRVS data of WT and C169 HYDA1 ^{57}Fe-labeled only at [2Fe] of (A) **Hox-CO**, (B) **Hox-O_2**, and (C) **HhydH**, compared to **Hox**. Middle: calculated spectra (x0.5) from QM/MM (TPSSh) for **Hox-CO** (apical CN^-), **Hox-O_2**, and **HhydH** with a proton at S9 (and **Hox-CO** with apical CO, dark-cyan; "**Hhyd**", light-green; Fig. 3). Experimental spectra were smoothed over ~10 cm^{-1}, calculated spectra are shown at a similar resolution. Bottom: experimental and calculated difference spectra (vertically shifted; **Hox-CO** (apical CO) – **Hox** and **Hhyd** – **Hox**, black lines). (D) Vibrational modes dominating spectral features marked a-g in panels A-C (arrows show vibrational amplitudes and directions, not drawn to scale).

Figure 5: Nuclear forward scattering time traces. Black lines, experimental data for HYDA1 variants labeled with ^{57}Fe only at [2Fe]; colored lines, simulation curves (Eq. 1) with parameters in Table 4 (transients normalized to a zero-time amplitude of unity).

Figure 6: X-ray pre-edge absorption and Kβ satellite emission. (A) Experimental pre-edge absorption (ctv) spectra for indicated Kβ emission detection energies (left and middle panels) and Kβ satellite emission (vtc) spectra (right panel). (B) Calculated (DFT/TPSSh, small models) ctv spectra for [2Fe] and [4Fe4S] (left and middle panels) and vtc spectra of the whole H-cluster (right panel). Magnified and shifted difference spectra shown at the bottom in panels in (A) and (B) (**HhydH** with protons at Fe_d and S9, for ctv/vtc spectra of further H-cluster species see Figs. S10, S11). (C) α LUMOs and HOMOs (β MOs in Fig. S12) and target or source MOs accounting for main ctv absorption or vtc emission features (a-c) in (B).

Figure 7: Spin and charge at the H-cluster. Data from DFT (TPSSh, small models) on indicated structures (Fig. 3) (A) Spin densities, (B) charge distribution at iron or iron/ligand groups, (C) mean frontier MO energies and energy gaps (bars = energy ranges of α and β spin MOs) and energy and gap differences, Δ = **Hi** – **Hox**) (4Fe = [4Fe4S] core excluding cys = cysteine ligands; api = apical CO, O_2, or H^+ ligand at Fe_d). (D) Spin density distribution.

Figure 8: H-cluster model structures. Structures of species (Fig. 3) from DFT (TPSSh, small models). Color code: white, H; grey, C; blue, N; red, O; yellow, S; orange, Fe. Bond lengths and distances (rounded, in Å) colored according to atom types (except for hydrogens, black numbers in italics), mean values over several distances (e.g. for Fe-Fe distances in [4Fe4S]) underlined, dashes mark (weak) H-bonding interactions. For further structures see Fig. S14.

Figure 9: H_2 conversion cycle in [FeFe]-hydrogenase. The three H-cluster species (4Fe = [4Fe-4S] complex, 2Fe = diiron complex) share an active site with a μCO ligand. Complex charges refer to added electrons/protons with the oxidized state, **Hox**, set to zero. The indicated reduction (-) at [4Fe4S] or [2Fe] agrees with the present and earlier data [29, 35, 39, 40, 42]. Protonation (H^+) at a cysteine ligand of [4Fe4S] is favored in the two-electron reduced **HhydH** and the one-electron reduced **Hred´ states** (this work and refs [29, 35]). If the second proton in H_2 does not correspond to the proton at [4Fe4S] in **HhydH**, a further oxidized intermediate (**HoxH**) with a proton at [4Fe4S] may be formed after delivery of two protons to [2Fe] and H_2 release, which deprotonates to form **Hox**, as suggested by our earlier studies [29]. **HhydH** accumulates under H_2 only for an impaired adt/C169 proton path. **HoxH** accumulates under reducing conditions for impaired [4Fe4S] deprotonation (at acidic pH) [29, 35]. Under physiological H_2 turnover conditions, the H-cluster therefore may cycle between **Hox** and **Hred´**.

Figure 1

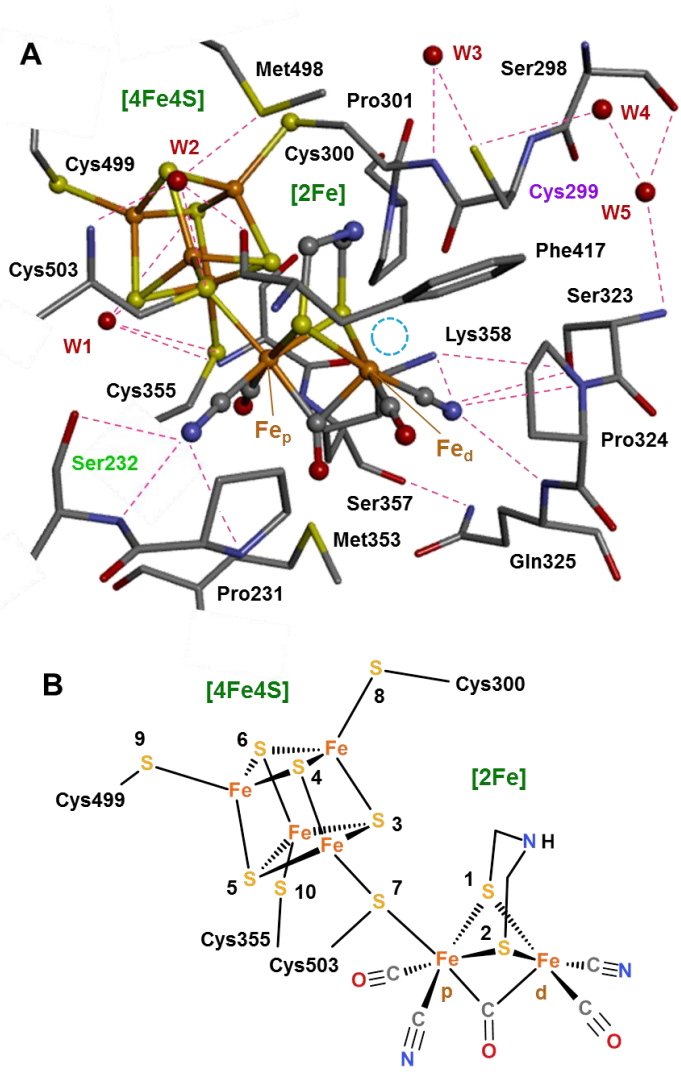
A
[4Fe4S]
Met498
Pro301
W3
Ser298
W4
W2
Cys499
Cys300
[2Fe]
Cys299
W5
Phe417
Cys503
Ser323
Lys358
W1
Cys355
Fe$_p$
Fe$_d$
Pro324
Ser232
Ser357
Met353
Gln325
Pro231
B
[4Fe4S]
Cys300
[2Fe]
Cys499
Cys355
Cys503
NH
p
d

Figure 2

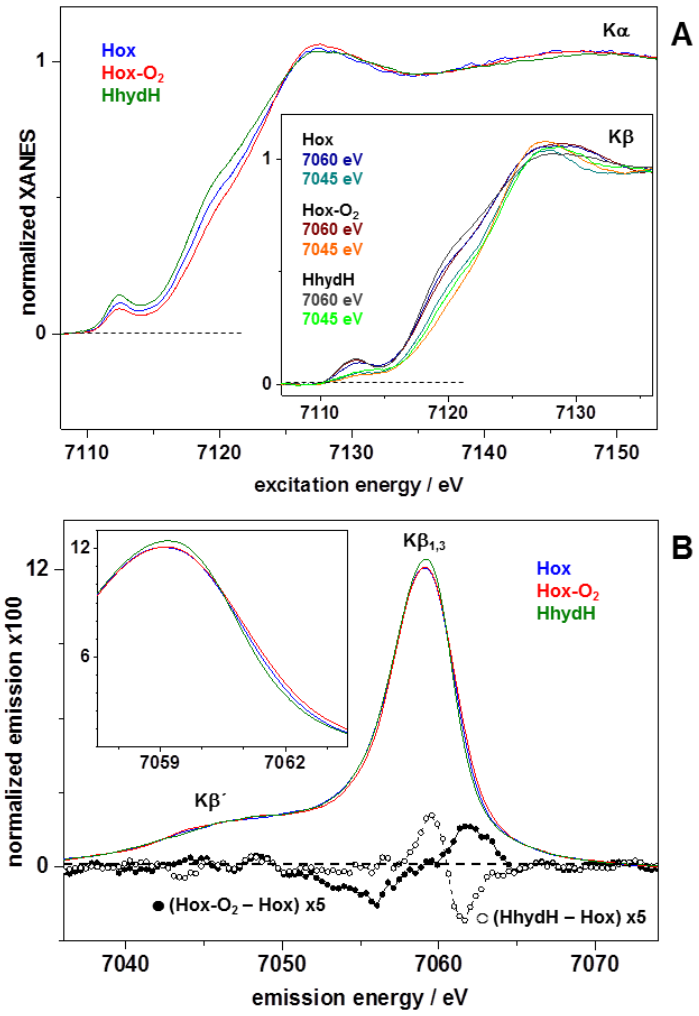
A
Kα
Hox
Hox-O2
HhydH
normalized XANES
1
0
7110
7120
7130
7140
7150
excitation energy / eV
Kβ
Hox
7060 eV
7045 eV
Hox-O2
7060 eV
7045 eV
HhydH
7060 eV
7045 eV
1
0
7110
7120
7130
B
Kβ1,3
Hox
Hox-O2
HhydH
12
6
7059
7062
Kβ´
normalized emission x100
12
0
● (Hox-O2 – Hox) x5
○ (HhydH – Hox) x5
7040
7050
7060
7070
emission energy / eV

Figure 3

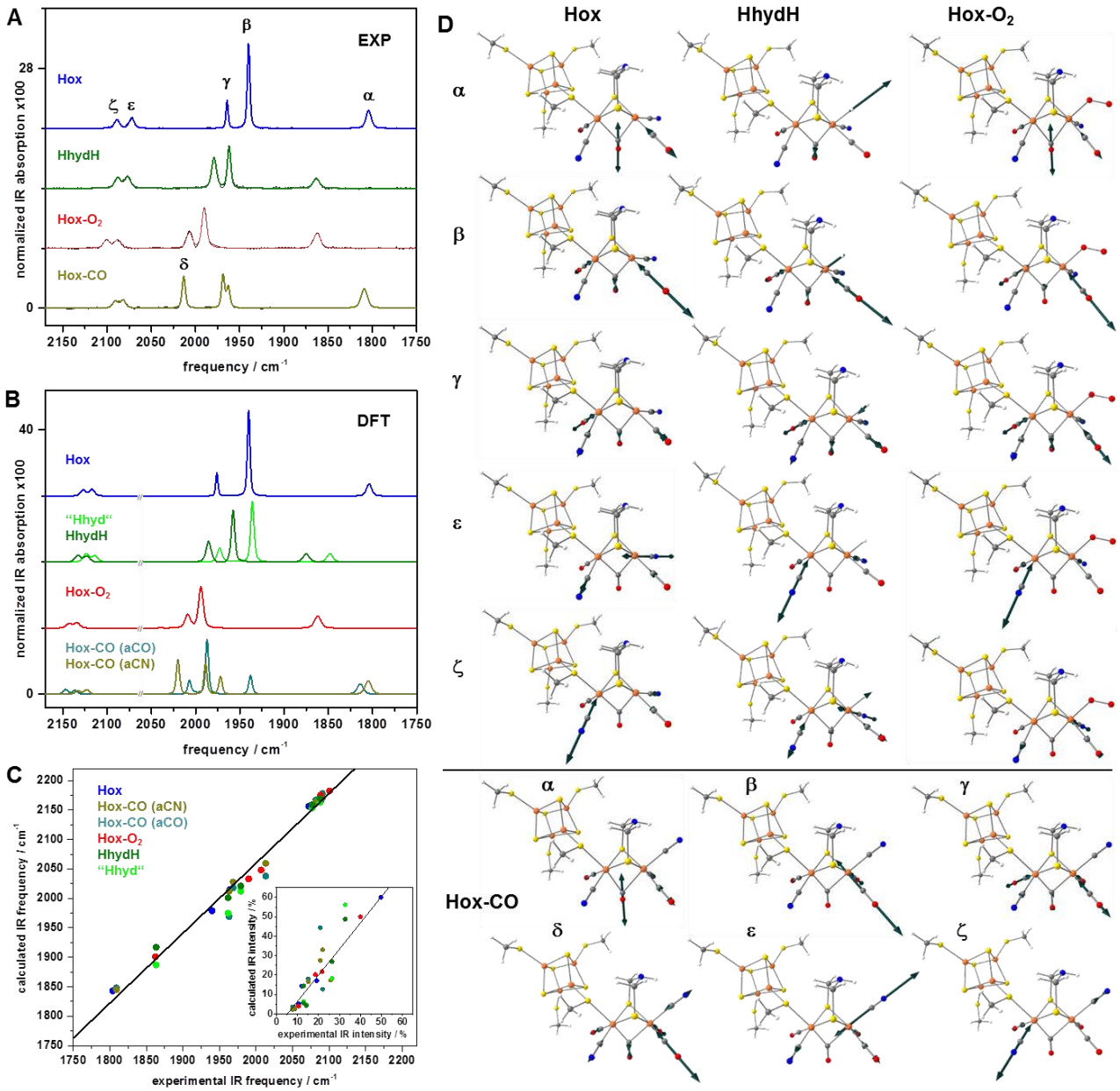
A
EXP
Hox
HhydH
Hox-O2
Hox-CO
ζ ε γ β α δ
normalized IR absorption x100
frequency / cm-1
B
DFT
Hox
"Hhyd"
HhydH
Hox-O2
Hox-CO (aCO)
Hox-CO (aCN)
normalized IR absorption x100
frequency / cm-1
C
Hox
Hox-CO (aCN)
Hox-CO (aCO)
Hox-O2
HhydH
"Hhyd"
calculated IR frequency / cm-1
experimental IR frequency / cm-1
calculated IR intensity / %
experimental IR intensity / %
D
Hox
HhydH
Hox-O2
α
β
γ
ε
ζ
Hox-CO
α
β
γ
δ
ε
ζ

Figure 4

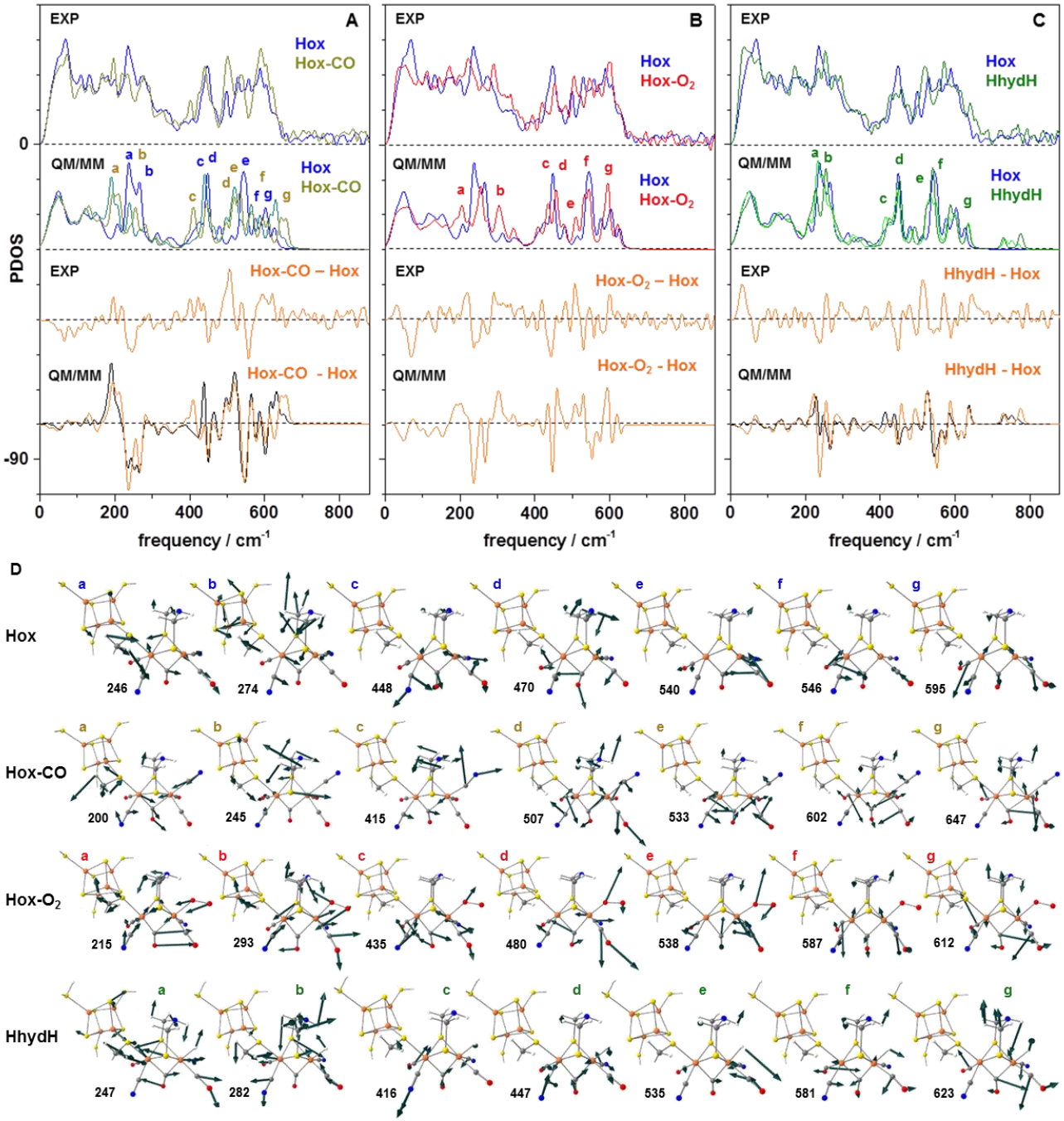
EXP
A
Hox
Hox-CO
QM/MM
Hox
Hox-CO
EXP
Hox-CO – Hox
QM/MM
Hox-CO - Hox
B
Hox
Hox-O2
Hox
Hox-O2
EXP
Hox-O2 – Hox
QM/MM
Hox-O2 - Hox
C
Hox
HhydH
Hox
HhydH
EXP
HhydH - Hox
QM/MM
HhydH - Hox
PDOS
0
-90
0
200
400
600
800
frequency / cm-1
D
Hox
246
274
448
470
540
546
595
Hox-CO
200
245
415
507
533
602
647
Hox-O2
215
293
435
480
538
587
612
HhydH
247
282
416
447
535
581
623

Figure 5

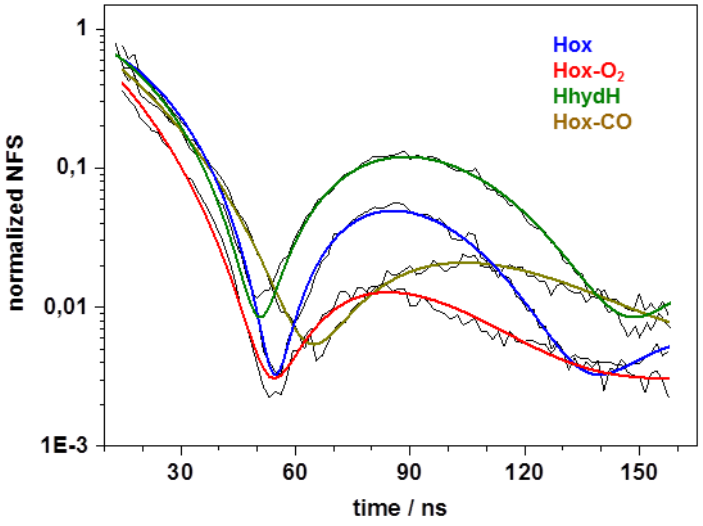
Hox
Hox-O2
HhydH
Hox-CO
normalized NFS
1
0,1
0,01
1E-3
30
60
90
120
150
time / ns

Figure 6

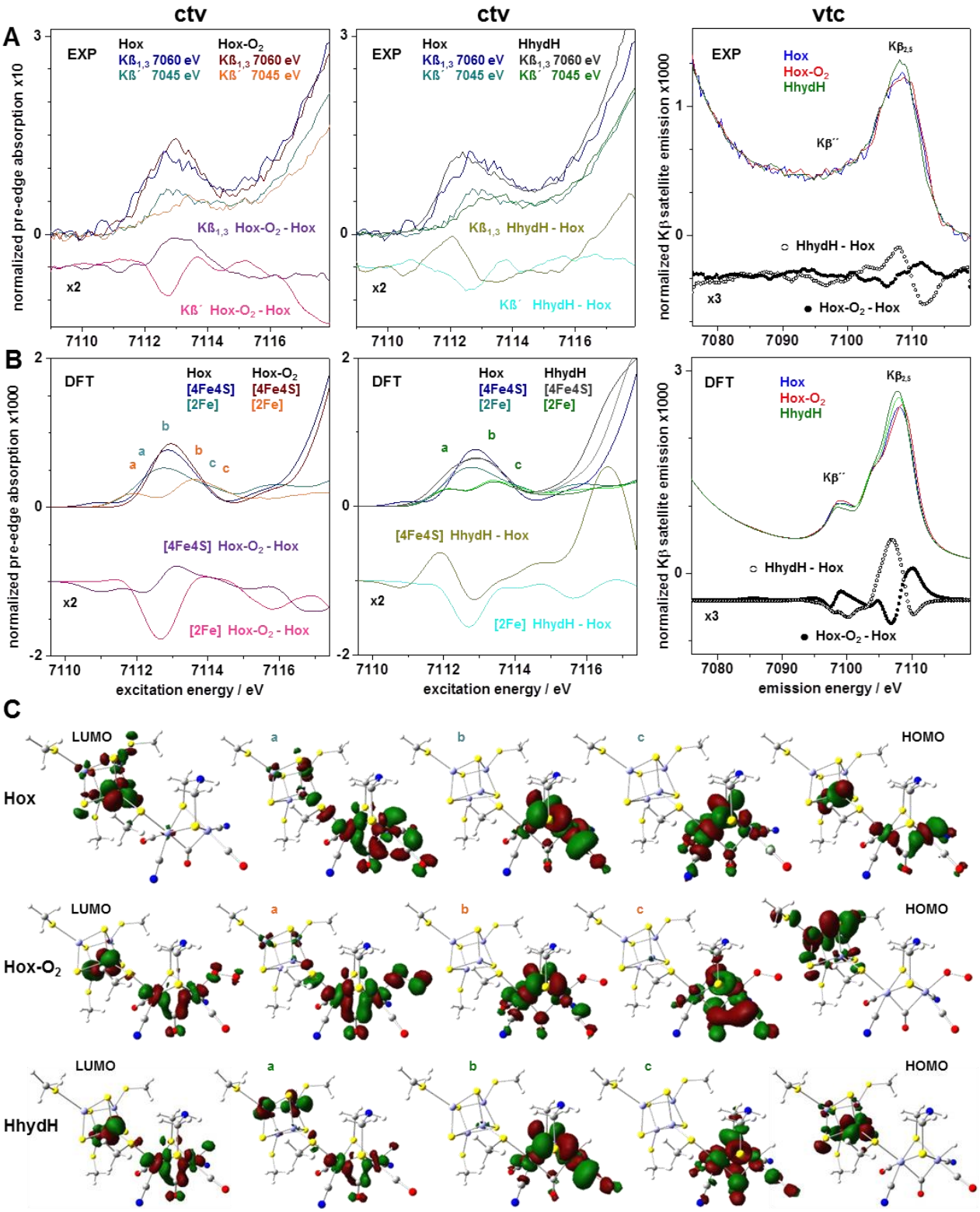
ctv
ctv
vtc
A
EXP
Hox
Kß1,3 7060 eV
Kß´´ 7045 eV
Hox-O2
Kß1,3 7060 eV
Kß´´ 7045 eV
HhydH
Kß1,3 7060 eV
Kß´´ 7045 eV
Kβ2,5
Kβ´´
Hox
Hox-O2
HhydH
normalized pre-edge absorption x10
normalized Kβ satellite emission x1000
Kß1,3 Hox-O2 - Hox
Kß1,3 HhydH - Hox
Kß´ Hox-O2 - Hox
Kß´ HhydH - Hox
HhydH - Hox
Hox-O2 - Hox
x2
x3
B
DFT
Hox
[4Fe4S]
[2Fe]
Hox-O2
[4Fe4S]
[2Fe]
HhydH
[4Fe4S]
[2Fe]
[4Fe4S] Hox-O2 - Hox
[2Fe] Hox-O2 - Hox
[4Fe4S] HhydH - Hox
[2Fe] HhydH - Hox
excitation energy / eV
emission energy / eV
C
Hox
Hox-O2
HhydH
LUMO
HOMO
a
b
c

Figure 7

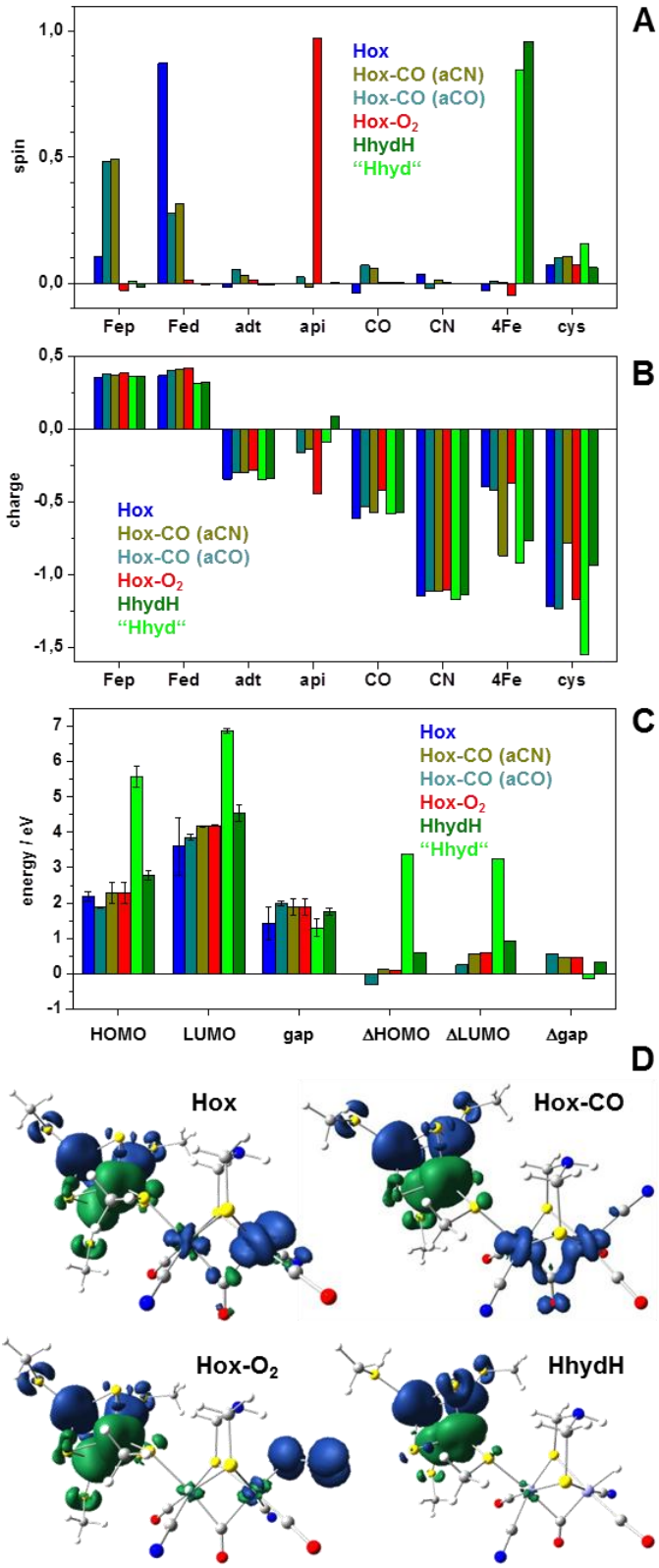
A
spin
1,0
0,5
0,0
Hox
Hox-CO (aCN)
Hox-CO (aCO)
Hox-O2
HhydH
"Hhyd"
Fep
Fed
adt
api
CO
CN
4Fe
cys
B
charge
0,5
0,0
-0,5
-1,0
-1,5
Hox
Hox-CO (aCN)
Hox-CO (aCO)
Hox-O2
HhydH
"Hhyd"
Fep
Fed
adt
api
CO
CN
4Fe
cys
C
energy / eV
7
6
5
4
3
2
1
0
-1
Hox
Hox-CO (aCN)
Hox-CO (aCO)
Hox-O2
HhydH
"Hhyd"
HOMO
LUMO
gap
ΔHOMO
ΔLUMO
Δgap
D
Hox
Hox-CO
Hox-O2
HhydH

Figure 8

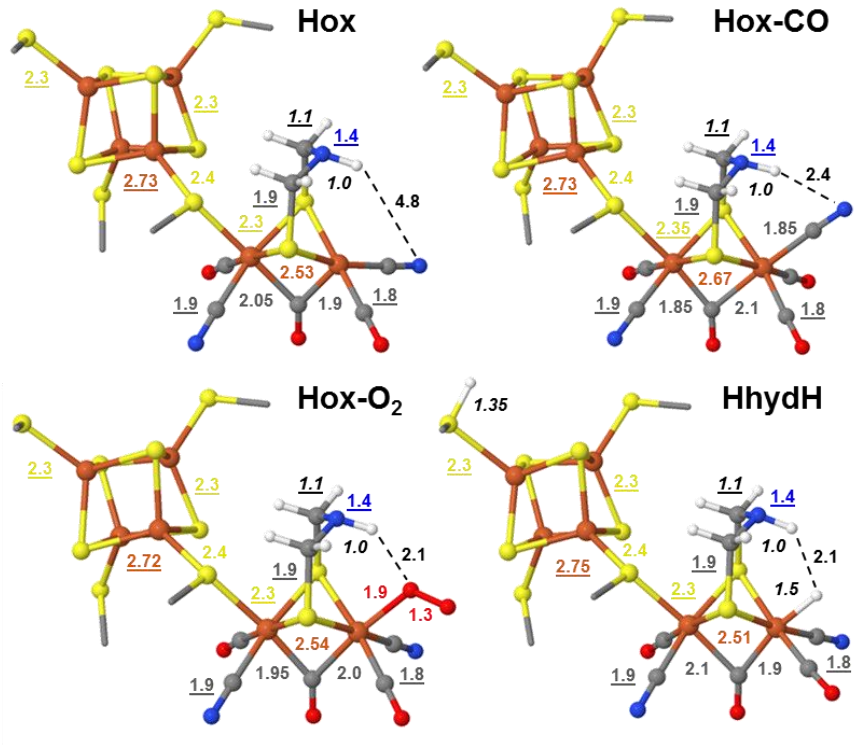
Hox
2.3
2.3
2.73
2.4
1.1
1.4
1.9
1.0
4.8
2.3
2.53
1.9
2.05
1.9
1.8
Hox-CO
2.3
2.3
2.73
2.4
1.1
1.4
2.4
1.0
1.9
2.35
1.85
2.67
1.9
1.85
2.1
1.8
Hox-O2
2.3
2.3
2.72
2.4
1.1
1.4
1.0
2.1
1.9
2.3
1.9
1.3
2.54
1.9
1.95
2.0
1.8
HhydH
1.35
2.3
2.3
2.75
2.4
1.1
1.4
1.0
2.1
1.9
2.3
1.5
2.51
1.9
2.1
1.9
1.8

Figure 9